



Almost all aspects of life are engineered at the molecular level, and without understanding molecules we can only have a very sketchy understanding of life itself. (Francis Harry Compton Crick)

16.1 Nuclear Cardiology

Coronary artery disease (CAD), stroke, and congestive heart failure (CHF) are responsible for the majority of all cardiovascular deaths. The current major diagnostic imaging procedures in nuclear cardiology to address the issues of CAD and heart failure are based on the assessment of myocardial blood flow (MBF) and substrate metabolism using FDA-approved SPECT and PET radiopharmaceuticals (Table 16.1). A number of review articles have extensively discussed various clinical issues and the relative significance of noninvasive imaging techniques in nuclear cardiology [1–4]. In the last 30 years, the application of qualitative perfusion imaging based on SPECT has been extended to allow for the combined evaluation of perfusion, perfusion reserve, and ventricular function. The coronary flow reserve (CFR) is a quantitative parameter defined by the ratio of maximal **myocardial blood flow** to the rest myocardial blood flow, which allows to give functional information on the whole coronary **arterial tree**, integrating both epicardial arteries and microcirculatory. The

CFR is a powerful tool to guide therapy and to assess prognosis [5]. With the improvements in SPECT instrumentation and with the availability of CZT-PECT and Dynamic PET scanners, the time has come for nuclear cardiology to provide the CFR measurements for clinical practice.

In cardiology, a paradigm shift is taking place with the emphasis from treatment to prevention of the disease. Current strategies involve the use of targeted markers of biological processes. With the recent advances in molecular biology, including genomics and proteomics, molecular imaging using biologically targeted radiopharmaceuticals will play a key role in this interdisciplinary approach to understanding the origins, pathogenesis, and progress of cardiac diseases, and in evaluating therapeutic interventions. Several molecular imaging radiopharmaceuticals with potential clinical utility are listed in Table 16.1. Today, molecular imaging of the heart is increasingly requested by cardiologists for infection, inflammation, infiltration, coronary atherosclerosis, vulnerable plaque, and heart failure. This trend is further fueled by the advent of an increasing spectrum of novel molecule-targeted drug interventions in cardiology, which require early identification of the most suitable patients and subsequent monitoring of success [4]. Several recent reviews discussed the potential clinical significance of different molecular imaging stud-

Table 16.1 Radiopharmaceuticals in nuclear cardiology

Assessment/mechanism	RP for SPECT	RP for PET
Myocardial perfusion/myocardial blood flow	^{201}Tl -chloride ^a	$^{[15]\text{O}}$ -water
	$^{99\text{m}}\text{Tc}$ -Sestamibi (Cardiolite TM) ^a	^{82}Rb chloride ^a
	$^{99\text{m}}\text{Tc}$ -Tetrofosmin (Myoview TM) ^a	$^{[13]\text{N}}$ Ammonia ^a
		$^{[18]\text{F}}$ -Flurpiridaz
Blood pool/ejection fraction	$^{99\text{m}}\text{Tc}$ -RBCs ^a	
Myocardial infarction	$^{99\text{m}}\text{Tc}$ -PYP ^a	
Glucose metabolism (viability)		$^{[18]\text{F}}$ Fluorodeoxyglucose (FDG)
Fatty acid metabolism	^{123}I -BMIPP	$^{[11]\text{C}}$ Palmitate
		$^{[18]\text{F}}$ FTHA
Oxidative metabolism		$^{[11]\text{C}}$ Acetate
Myocardial sympathetic innervation	^{123}I -MIBG (Iobenguane)	$^{[11]\text{C}}$ meta-hydroxyephedrine (HED)
β -adrenergic receptors		$^{[11]\text{C}}$ CGP12177
Infection/inflammation	^{111}In or $^{99\text{m}}\text{Tc}$ labeled leukocytes	$^{[18]\text{F}}$ FDG
Cardiac sarcoidosis	^{111}In -DTPA-Octreotide (Octreoscan)	$^{[18]\text{F}}$ FDG
		$^{[18]\text{F}}$ Fluorothymidine (FLT)
		^{68}Ga -Dotatate; ^{68}Ga -Dotatoc
Cardiac amyloidosis	$^{99\text{m}}\text{Tc}$ -PYP	$^{[11]\text{C}}$ PiB, $^{[18]\text{F}}$ Flutemetamol
	$^{99\text{m}}\text{Tc}$ -HMDP	$^{[18]\text{F}}$ Florbetaben
	$^{99\text{m}}\text{Tc}$ -DDP	$^{[18]\text{F}}$ Florbetapir
	$^{99\text{m}}\text{Tc}$ -Aprotinin	
Fibrosis: fibroblast activating protein (FAP)		^{68}Ga -FAPi-04
Atherosclerosis		$^{[18]\text{F}}$ FDG
		$^{[18]\text{F}}$ Fluoride
Inflammatory pathway: chemokine receptor (CXCR4)	^{111}In -Pentixafor	^{68}Ga -Pentixafor

DPD = 3,3-diphosphono-1,2-propanodicarboxylic acid

^aFDA approved agents

ies that are in clinical use and the new, and novel agents under investigation [4, 6–9].

16.2 The Clinical Problem

16.2.1 Coronary Artery Disease

The coronary arteries originate from the left and right coronary sinuses of the aorta (Fig. 16.1). The left main coronary artery divides into two major arteries: the left anterior descending artery (LAD) and the left circumflex artery (LCx). The right coronary artery (RCA) divides into a posterior descending artery (PDA) and a posterior left ventricular branch. The cardiac muscle has two

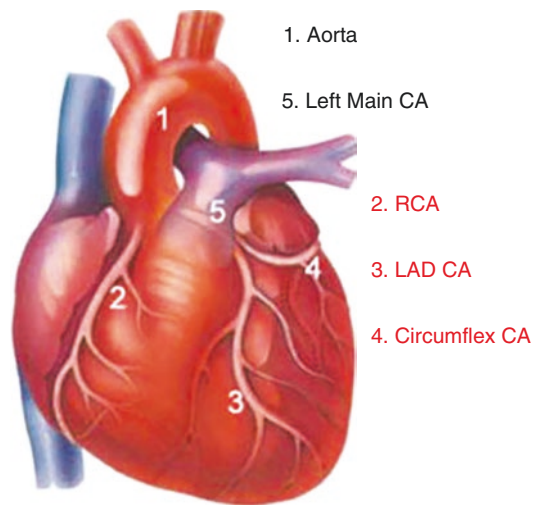


Fig. 16.1 Heart with coronary arteries

essential properties: electrical excitability and contractility. The ability of myocardial muscle cells to contract and generate the force necessary to maintain blood circulation is achieved through the unique contractile function of two proteins of the sarcomere (actin and myosin) of the syncytially arranged myocardial fibers. Also, the heart muscle has a rich supply of the high-energy phosphates needed for the contraction.

The majority of patients with acute coronary syndromes (ACS) present with unstable angina, acute myocardial infarction, and sudden coronary death. The disease may be asymptomatic until advanced in severity or complications. CAD is an immune inflammatory process, which, over decades, results in arterial narrowing [10, 11]. Atherosclerosis is a systemic disease with focal manifestations, and it is by far the most frequent underlying cause of CAD. It is also a complex

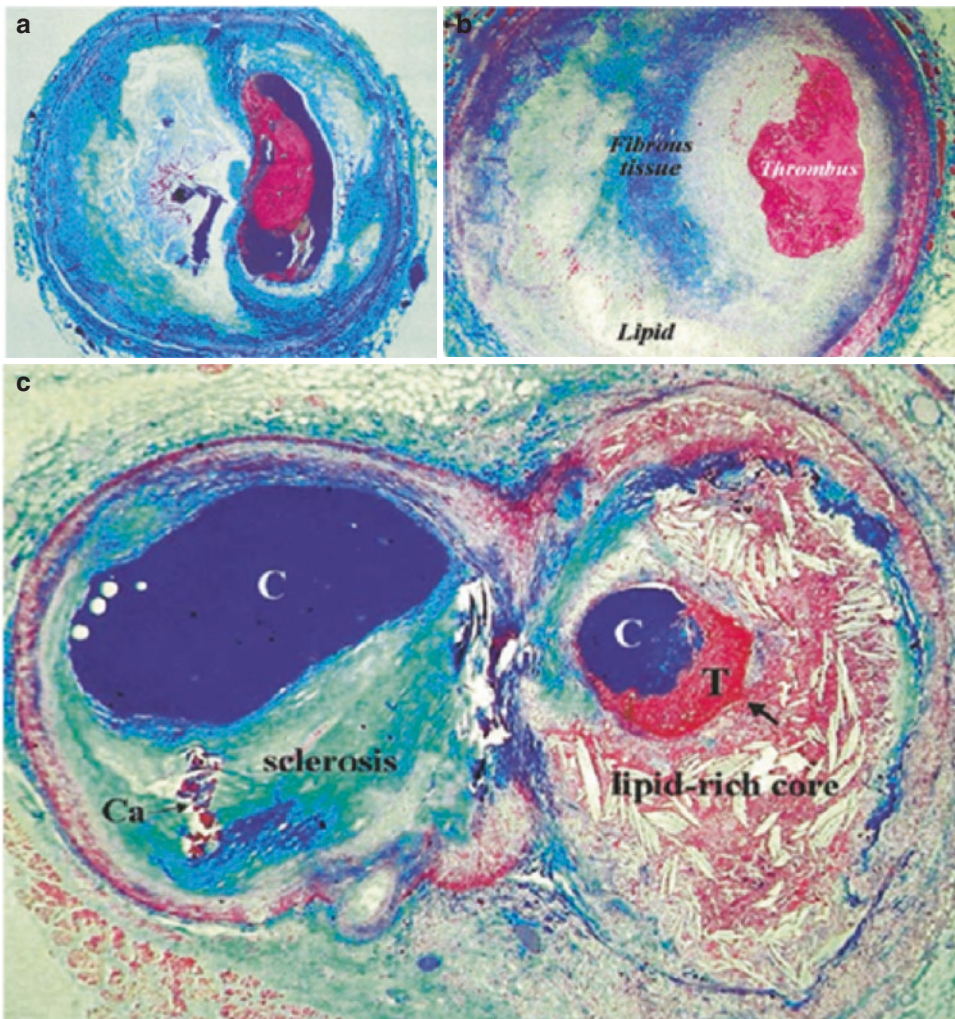


Fig. 16.2 Atherosclerosis and thrombosis in coronary arteries (CA): (a) cross-sectioned CA containing a ruptured plaque with a nonocclusive platelet-rich thrombus superimposed; (b) cross section of a CA containing a stenotic atherosclerotic plaque with an occlusive thrombosis superimposed (plaque erosion); (c) atherothrombosis: a variable mix of chronic atherosclerosis and acute throm-

bosis. Cross-sectioned arterial bifurcation illustrating a collagen-rich (*blue-stained*) plaque in the circumflex branch (*left*) and a lipid-rich and ruptured plaque with a nonocclusive thrombosis superimposed in the obtuse branch (*right*). *C* contrast in the lumen, *Ca* calcification, *T* thrombosis [12]

disease in which cholesterol deposition, inflammation, and thrombus formation play a major role. Atherosclerotic lesions (Fig. 16.2), according to the American Heart Association classification are divided into two groups: nonatherosclerotic intimal lesions and progressive atherosclerotic lesions [13]. A third group of lesions, healed atherosclerotic plaques, are the most prevalent lesions, particularly in the carotid arteries. A variety of factors contribute to the development and progression of atherosclerosis. Dysfunction of the endothelium, which maintains vascular homeostasis by regulating vascular tone, smooth muscle cell proliferation, and thrombogenicity, is thought to be the earliest step in the development of CAD. The endothelial dysfunction results in the imbalance of vascular regulatory mechanisms to cause damage to the arterial wall. Inflammation, macrophage infiltration, lipid deposition, calcification, extracellular matrix digestion, oxidative stress, cell apoptosis, and thrombosis are among other molecular mechanisms that contribute to plaque development and progression [10, 14, 15]. The practice of estimating the severity of atherosclerotic disease by using CT calcification was introduced in the 1980s and was standardized with the publication of a CT calcium score. The utility in early diagnosis is limited by the fact that the macrocalcifications visible on CT are a relatively late-

stage manifestation of atherosclerosis. By contrast, molecular imaging techniques can theoretically visualize the preliminary stages and microscopic manifestations of the disease process (such as inflammation, microcalcification) and, if validated, would constitute an ideal modality for early diagnosis and intervention [8].

Atherosclerosis, alone, is rarely fatal; it is thrombosis, superimposed on a ruptured or eroded atherosclerotic plaque, that precipitates life-threatening clinical events, such as acute coronary syndromes (ACS) and stroke [14]. Therefore, the term atherothrombotic disease is more appropriate since the atherosclerotic and the thrombotic processes are interdependent [12].

16.2.1.1 Vulnerable Plaque

Since the 1970s, scientists have sought to find the mechanisms responsible for converting chronic coronary atherosclerosis to acute coronary artery disease. Despite major advances in the treatment of coronary heart disease patients, a large number of victims of the disease, who are apparently healthy, die suddenly without prior symptoms. In the 1990s the term *vulnerable plaque* was introduced to describe the rupture prone plaques as being the underlying cause of most clinical coronary events [16]. Based on histopathological observations, a nonthrombosed lesion, that most resembles the acute plaque rupture, has been

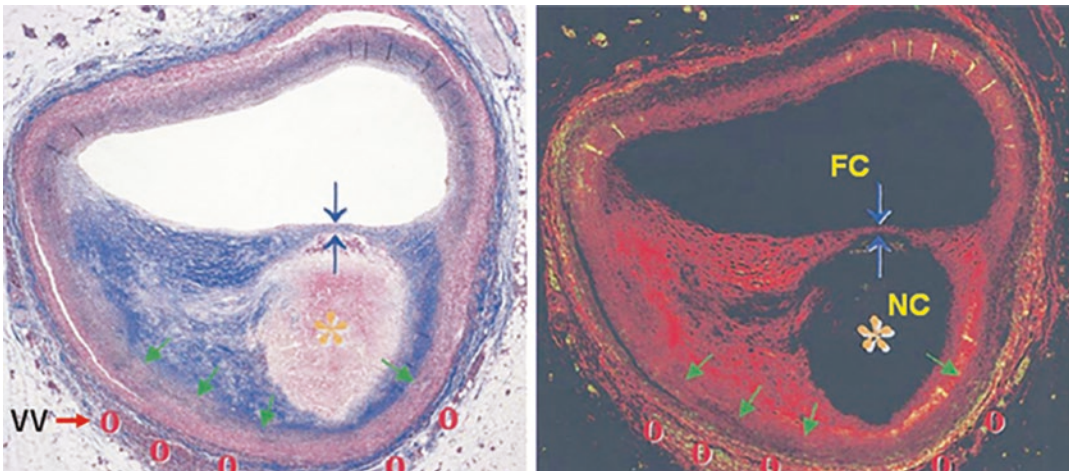


Fig. 16.3 Vulnerable plaque: cross section of a coronary artery containing plaque assumed to be rupture-prone containing a large lipid-rich necrotic core (NC), thin

fibrous cap (FC), expansive remodeling (*green arrow*), and vasa vasorum and neovascularization (VV) [14]

identified as the thin cap fibroatheroma (TCFA), which is characterized by a necrotic core with an overlying fibrous cap measuring $<65\ \mu\text{m}$, containing rare smooth muscle cells and numerous macrophages (Fig. 16.3) [14, 15]. An inflamed TCFA is suspected to be a high risk/vulnerable plaque [17, 18].

Stable plaques are characterized by intimal thickening associated with lipid deposition, a chronic inflammatory infiltrate but, without evidence of necrosis, whereas vulnerable and ruptured plaques are characterized by an “active” inflammation involved in the thinning of the fibrous cap, predisposing the plaque to rupture [13, 17]. Since rupture-prone plaques are not the only vulnerable plaques, it was proposed that all types of atherosclerotic plaques, with a high likelihood of thrombotic complications and rapid progression, should be considered as vulnerable plaques [19]. In addition, since the vulnerable blood (prone to thrombosis) and vulnerable myocardium (prone to fatal arrhythmia) play an important role in the clinical outcome, the term “vulnerable patient” has been regarded as being more appropriate [20, 21].

Molecular imaging of inflammation, atherosclerosis/atherothrombosis, and vulnerable plaque would play a major role in nuclear cardiology in the near future ([4, 6, 8, 19, 22, 23].

16.2.1.2 Myocardial Infarction

Myocardial infarction (MI) occurs in the setting of an acute coronary vessel occlusion, with a variable amount of spasm, and increased myocardial demand as contributing factors. Most of the ACS are thought to be the result of sudden luminal thrombosis which occurs from three different pathologies: plaque rupture, erosion, and calcified nodules [15]. Histopathological studies reveal a large peripheral zone infiltrate by neutrophils that surround the subendocardial central zone devoid of neutrophils. The perinfarct zone is a complex collection of regions in different states of injury, depending on the amount of blood flow reduction, myocardial metabolic demand, and the rate of onset and duration of the blood flow reduction. Myocardial

necrosis and severe acute ischemia lead to increased permeability, cell membrane disruption, and leakage. Different myocardial tissue states or zones, such as hibernating and stunned myocardium, may be present depending on the extent of damage, viability, and function [23]. The hibernating myocardium is the term applied to a dysfunctional myocardium with reduced perfusion (ischemia) at rest, but preserved cell viability.

16.2.2 Congestive Heart Failure

CHF stems from inadequate cardiac output, due to systolic or diastolic left ventricular function. The primary causes are ischemic heart disease and hypertension. Both, idiopathic cardiomyopathy (ICM) and ischemic cardiomyopathy (ISM) are widespread and are major underlying cardiac diseases responsible for heart failure. Besides the risk of sudden cardiac death, patients with CHF can have intraventricular dyssynchrony (or left bundle branch block), which causes the two ventricles to beat in an asynchronous fashion, reduces systolic function, and increases systolic volume. Autonomic dysfunction has been shown to increase the risk of death in patients with heart disease and may be applicable to all patients with cardiac disease, regardless of etiology [24]. The impaired cardiac presynaptic function has pathophysiological implications in the occurrence of lethal cardiac events in patients with heart failure.

The autonomic innervation of the heart is the primary extrinsic control mechanism regulating cardiac performance. The heart is innervated by the parasympathetic and sympathetic nerve fibers. The left ventricle of the heart is primarily supplied by sympathetic nerves that modify cardiovascular performance in adapting to the changing hemodynamic requirements. The parasympathetic nervous system primarily innervates the atria and the conduction system. The major neurotransmitters of the sympathetic and parasympathetic systems are norepinephrine and acetylcholine, which define the stimulatory and

inhibitory physiological effects of each system. There is a highly regulated balance in the sympathetic and parasympathetic input to optimize cardiac performance.

16.2.3 Cardiomyopathy

Cardiomyopathy is a diseased heart muscle that cannot function (contract) adequately and results in the failure of the heart muscle to meet the needs of the body for oxygen-rich blood and the removal of carbon dioxide, and other waste products. There are many causes of cardiomyopathy but, the end result is a heart that is weak and cannot maintain a normal ejection fraction or cardiac output. Primary cardiomyopathies are those that usually affect the heart alone. Secondary cardiomyopathies (such as sarcoidosis and amyloidosis) are those that are a result of an underlying condition affecting many areas of the body [25, 26].

16.2.3.1 Cardiac Sarcoidosis (CS)

Sarcoidosis is a systemic inflammatory disorder resulting from the combined effects of genetic susceptibility and environmental exposures. Sarcoidosis is a granulomatous disease that affects multiple organs and has no clearly defined etiology. Although much attention is focused on lymphocytes in directing inflammation in sarcoidosis, macrophages remain the dominant constituent of the sarcoidosis granuloma. The cardiovascular system is the third most common site of sarcoidosis and is involved in 25–50% of patients. Patients with heart failure have a particularly poor prognosis [25, 91]. The prevalence of sarcoidosis-related cardiomyopathy is increasing. Sarcoidosis impacts cardiac function through granulomatous infiltration of the heart, resulting in conduction disease, arrhythmia and/or heart failure. Diagnosis of CS can be challenging and requires clinician awareness as well as differentiation from overlapping diagnostic phenotypes such as other forms of myocarditis and arrhythmogenic cardiomyopathy [25]. Early diagnosis is the key to preventing the potentially devastating effects of cardiac sarcoidosis (CS).

Cardiac MRI offers high spatial resolution and enables evaluation of ventricular function, myocardial edema, and scarring. It provides high diagnostic value (sensitivity, 76–100%; specificity, 78–92%). However, contrast-enhanced cardiac MRI cannot be performed in patients with implantable devices and/or severe renal impairment [91]. Molecular imaging with PET radiotracers has the advantages of overcoming these disadvantages of cardiac MRI and provide definitive diagnosis of CS.

16.2.3.2 Cardiac Amyloidosis (CA)

CA is an infiltrative and restrictive cardiomyopathy that leads to heart failure, reduced quality of life, and death. CA is a disorder characterized by deposition of insoluble protein fibrils (i.e., amyloid) in the extracellular space. Fibrils from two protein precursors, amyloid immunoglobulin light chain (AL) and amyloid transthyretin (ATTR), are the main causes of cardiac amyloidosis [26]. Based on the protein fibrils, CA is categorized into two subtypes, transthyretin cardiac amyloidosis (ATTR-CA) and immunoglobulin light chain cardiac amyloidosis (AL-CA), characterized by the precursor protein that forms amyloid and infiltrates the myocardium. AL amyloidosis develops after deposition of misfolded proteins that originate from the AL fragments that are typically produced by bone marrow plasma cells. ATTR amyloidosis is caused by accumulation of transthyretin (TTR), a serum transport protein for thyroid hormone and retinol synthesized originally by the liver, and is classified into two subtypes: wild-type (ATTRwt-CA) and hereditary, previously called familial CA and now referred to as variant transthyretin CA (ATTRv-CA) [26]. CA is caused by cumulative myocardial deposition of insoluble amyloid that causes chamber stiffening, conduction disturbances, impaired diastolic function initially, and heart failure with preserved ejection fraction (HfpEF) that can progress to a reduced ejection fraction (EF). Transthyretin (alternatively, prealbumin) is a tetrameric protein mainly produced in the liver that transports thyroid hormone and retinol. With aging, or a destabilizing mutation, the tetramer dissociates into monomers

or oligomers that misfold and aggregate into amyloid fibrils.

Recent advances in therapeutic options render accurate and early diagnosis of CA critical. Previously, definitive diagnosis of ATTR-CA often required an endomyocardial biopsy staining positive with Congo Red, with confirmatory testing for ATTR via immunohistochemistry or serum/urine protein electrophoresis with immunofixation mass spectroscopy. Endomyocardial biopsy is highly sensitive and specific (nearly 100% for each) and is considered the gold standard for diagnosis [26]. However, given its invasive nature, biopsy was performed only when there was significant suspicion of CA. Radionuclide planar/SPECT imaging studies with ^{99m}Tc bone agents or β -amyloid binding PET radiotracers can provide non-invasive diagnostic information.

16.2.4 Fibrosis

Postinfarction remodeling involves infiltration of activated fibroblasts into affected myocardium to assist with repair and to maintain structural integrity of affected tissue. Myocardial fibrosis is a common endpoint of cardiovascular disease, characterized by resident cardiac fibroblast trans-differentiation and activation, which produce fibrillary collagen and reorganize extracellular matrix. Reparative or replacement fibrosis after ischemic injury culminates in scar formation and stabilization of the infarct [27]. The dynamic remodeling process is driven by a multitude of cells including cardiomyocytes, endothelial cells, immune cells, and cardiac fibroblasts. After MI, fibroblasts undergo dynamic phenotypic changes and differentiate into collagen-secreting proto-myofibroblasts. These activated fibroblasts can further differentiate into mature myofibroblasts. After MI, activated fibroblasts migrate into the injured myocardium and contribute to tissue replacement, thereby helping to preserve the structural integrity of the infarcted heart. They secrete increased amounts of cytokines, growth factors, and pericellular proteases to maintain the extracellular matrix (ECM) and promote replace-

ment fibrosis—formation of a scar that stabilizes the ventricular wall and maintains the macroanatomy of the heart [28]. Excessive fibrosis, however, can lead to left ventricular stiffness, decreased contractility, and ultimately contributes to the progression to HF. Noninvasive imaging of activated fibroblasts could therefore provide unique opportunities to study cardiac remodeling over time and to monitor therapeutic interventions that aim to prevent a progressive decline of ventricular function [29, 30].

16.3 Radiopharmaceuticals in Nuclear Cardiology

SPECT and PET radiopharmaceuticals with specific clinical applications in cardiology are summarized in Table 16.1. The mechanisms of uptake and clinical utility of both approved and investigational radiopharmaceuticals will be described briefly in the following sections.

16.3.1 Myocardial Blood Flow/Perfusion

Myocardial perfusion Imaging (MPI) with SPECT has been the clinical workhorse for MPI, but over the past two decades, PET MPI is experiencing growth due to enhanced image quality that results in superior diagnostic accuracy over SPECT. Furthermore, dynamic PET imaging of the tracer distribution process from the time of tracer administration to tracer accumulation in the myocardium has enabled routine quantification of myocardial blood flow (MBF) and myocardial flow reserve (MFR) in absolute units [31].

MBF is regulated by anatomical, hydraulic, mechanical, and metabolic factors. Autoregulation of MBF is driven by changes in regional myocardial metabolism and oxygen consumption. Under resting conditions, MBF is one-fifth the maximum flow capacity, which occurs during reactive hyperemia and, or with maximum pharmacological vasodilation [32]. Near-maximal MBF can be produced by intense metabolic stress associated with exercise. The difference between the peak

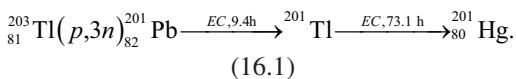
(under stress) and basal MBF represents the coronary flow reserve (CFR), which is reduced in the presence of severe CAD.

The resting MBF is not reduced until the stenosis exceeds 90% of the normal vessel diameter. The coronary flow reserve, however, is reduced with only a 50% diameter stenosis [33]. Therefore, myocardial perfusion imaging (MPI) is performed in conjunction with exercise or pharmacological vasodilatation (using adenosine, dipyridamole, or dobutamine) in order to identify subcritical coronary stenosis. MPI maps the relative distribution of coronary flow, which is normally almost uniform in the absence of prior infarction or fibrosis.

The ideal MPI radiopharmaceutical should have a linear relationship between myocardial uptake and blood flow, high first-pass extraction over a wide range of blood flow rates, low extracardiac uptake, minimal myocardial redistribution, and intrinsic chemical stability. The relationship between uptake and clearance of the radiotracer and MBF should be constant and independent of MBF, physiological and pathological changes of the myocardial tissue state, and the myocardial metabolism. Most radiotracers used for imaging the myocardial perfusion/blood flow, however, do not fully meet these requirements [2, 34].

16.3.1.1 SPECT Radiotracers for Perfusion

^{201}Tl as thallos chloride behaves like a K^+ analog and is highly extracted by the myocardial cell. It was first introduced in the 1970s as a radiopharmaceutical for myocardial perfusion imaging [35]. ^{201}Tl , with a physical half-life of 73.1 h, decays by electron capture to ^{201}Hg , which emits useful X-ray photons (69–80 KeV; 94.4% abundance) for gamma camera imaging studies. It is produced in a cyclotron and is indirectly based on the following nuclear reaction:



Following intravenous administration, it is rapidly cleared from the circulation and normal

myocardial tissue extracts about 85% of the amount present in the coronary arteries. At pH 4–7, ^{201}Tl predominantly exists as a monocation, and like K^+ ion, it relies on cell-membrane integrity and active metabolic transport using Na^+/K^+ pump for its uptake into the myocardial cells. Approximately 3–5% of the injected dose localizes in the normal myocardial tissue and after initial localization, there is rapid redistribution of ^{201}Tl activity in the myocardium. Early stress-induced defects, which later normalize in redistribution images, imply myocardial ischemia, while persistent defects indicate scarring.

Three important $^{99\text{m}}\text{Tc}$ labeled radiopharmaceuticals (Fig. 16.4) were introduced for myocardial perfusion imaging studies [36]; sestamibi (cardiolite[®]), tetrofosmin (MyoviewTM), and teboroxime (CardioTec), however, CardioTec is no longer commercially available. In the case of $^{99\text{m}}\text{Tc}$ -Sestamibi, six molecules of MIBI (2-methoxy isobutyl isonitrile) bind to the central $^{99\text{m}}\text{Tc}$ atom forming a coordination complex with a single positive charge. As a cationic complex, it is transported into the myocardium by passive diffusion (extraction efficiency < 60%), and the myocardial retention is due to mitochondrial binding. Tetrofosmin ($^{99\text{m}}\text{Tc}$ -1,2-bis[bis(2-ethoxyethyl)phosphino]ethane) is also a monocation complex and is transported into the myocardial tissue similar to sestamibi.

16.3.1.2 PET Radiotracers for Perfusion

Several PET radiopharmaceuticals are available for evaluating the relative distribution of MBF and for measuring regional MBF in absolute quantitative units (mL/min/g) based on PET [2, 31].

As described previously, the first-pass unidirectional extraction fraction E is the fraction of the tracer that changes across the capillary membrane during a single transit of tracer bolus through the coronary circulation. For most diffusible radiotracers, such as [^{15}O]water, $E < 1$ declines with increasing MBF. The relationship between E and the permeability-surface product and blood flow is described by Renkin and Crone. It is also important to note that the E for radio-

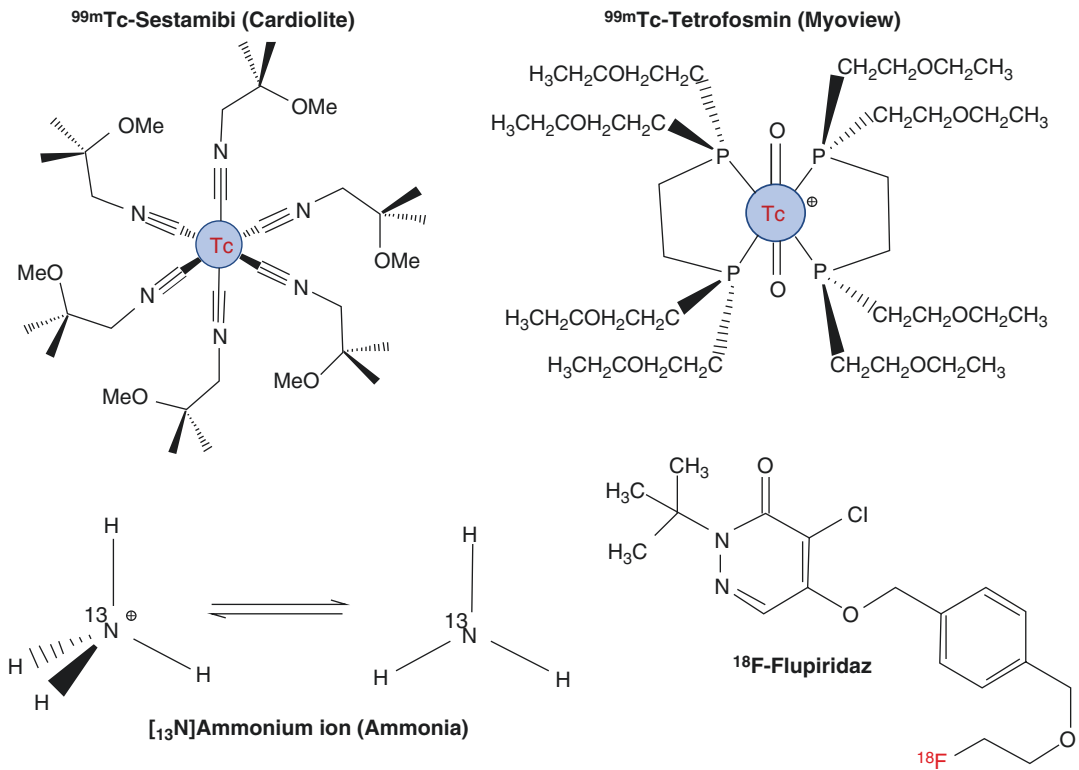


Fig. 16.4 SPECT and PET radiopharmaceuticals for myocardial perfusion imaging

tracers administered as bolus is generally higher than the steady state extraction fraction, also called the extraction ratio [34]. Also, the first-pass retention fraction R of the radiotracer may decrease at higher flow rates due to back diffusion of the radiotracer into the vascular space and blood. The plot of the myocardial net uptake ($E \times F$) for several radiotracers, as a function of MBF (Fig. 16.5), suggests that the net uptake would increase linearly with higher blood flows but, correlates nonlinearly with blood flow, except for [¹⁵O]water.

[¹⁵O]water meets the criteria for an ideal radiotracer for MBF measurement most closely. Based on a single tissue compartment model, MBF ($\text{mL min}^{-1} \text{g}^{-1}$) estimates in normal human subjects are 0.90 ± 0.22 at rest and 3.55 ± 1.15 with stress, based on intravenous dipyridamole [34].

[¹³N]Ammonia (NH_3) in circulation exists predominantly as an ammonium ion NH_4^+ at normal pH. It may be actively transported into the myocardial cells via the Na^+/K^+ pump or by the pas-

sive diffusion of neutral lipid-soluble ammonia. Inside the cell, ammonia is quickly converted to ammonium ion which is rapidly converted and trapped as glutamine by the enzyme *glutamine synthase* [34]. Because of the large intracellular levels of glutamine, the washout of N-13 activity from the cell is minimal. Since the rate of their back-diffusion depends on MBF, the retained fraction R declines with higher flow.

Intrasubject comparison studies have demonstrated a close linear correlation between MBF estimates determined by [¹⁵O]water and [¹³N] ammonia techniques, over a range of flows from 0.5 to 5.0 $\text{mL min}^{-1} \text{g}^{-1}$ [37]. Also, global and regional MBF estimates with [¹³N] ammonia have shown a close correlation to MBF estimates which were determined based on the inert argon gas washout technique [38]. In patients with CAD and previous myocardial infarctions, MBF estimates with [¹³N] ammonia and [¹⁵O]water may markedly differ in regions of previously infarcted myocardium [34]. MBF imaging with

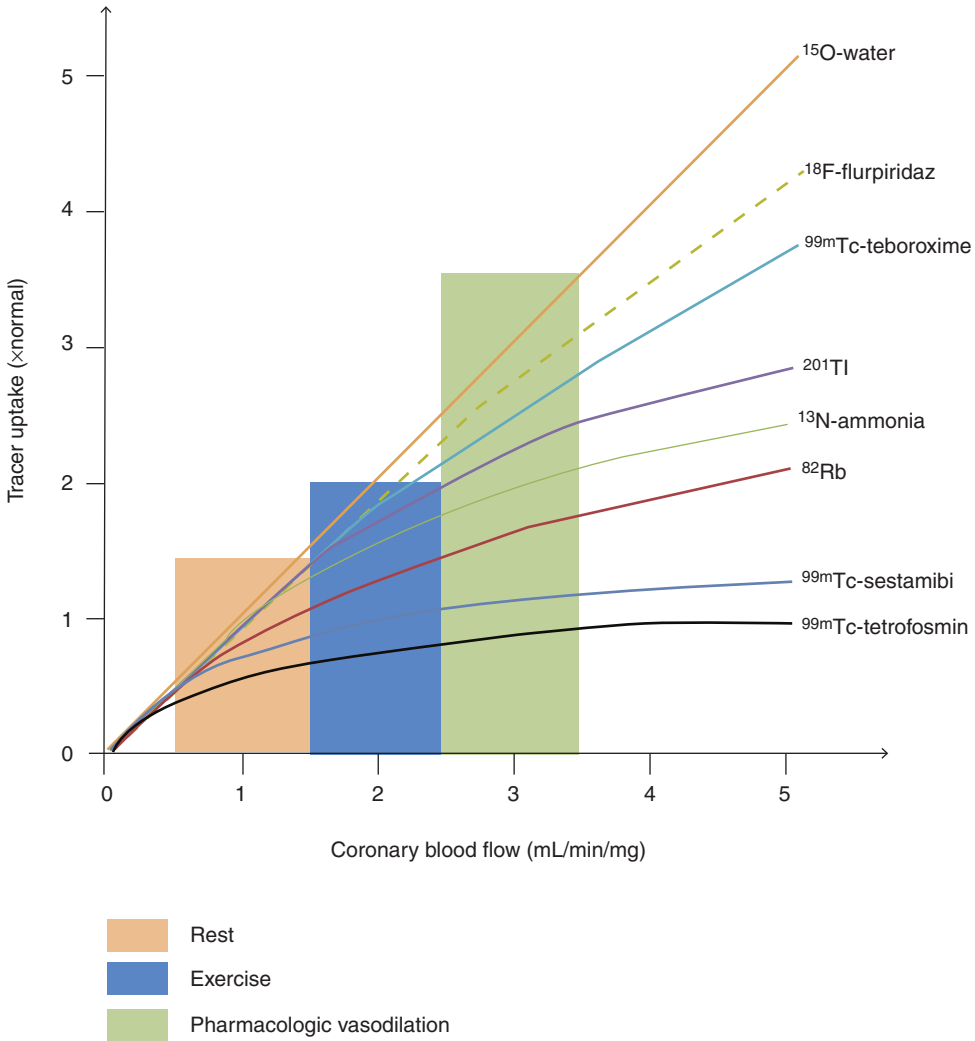


Fig. 16.5 Schematic representation of cardiac PET and SPECT radiotracers uptake in relation to myocardial perfusion. ^{15}O demonstrates close to linear uptake whereas the initial linear extraction of $^{99\text{m}}\text{Tc}$ labeled compounds plateau at approximately 2 mL/min/g. PET radio-

tracers $^{13}\text{NH}_4^+$ ion and $^{82}\text{Rb}^+$ fall between $^{201}\text{Tl}^+$ and the $^{99\text{m}}\text{Tc}$ -SPECT radiotracers, whereas $^{99\text{m}}\text{Tc}$ -teboroxime (discontinued) demonstrates superior extraction at high flow rates. ^{18}F Flurpiridaz rivals ^{15}O with closer to linear extraction. (From [31])

^{13}N ammonia-PET, demonstrating anterior and lateral defects, is shown in Fig. 16.6.

$^{82}\text{Rb}^+$ as a K^+ analog, is actively transported into the myocardial cells via the Na^+/K^+ pump. The extraction fraction decreases at high flows and can be altered by drugs, severe acidosis, hypoxia, and ischemia. $^{82}\text{Rb}^+$ appears to leak from the irreversibly injured myocardium, but is retied or continues to accumulate in only reversibly injured myocardium [34]. In normal sub-

jects, at baseline, and with dipyridamole stress, there is a close correlation between MBF estimates with $^{82}\text{Rb}^+$ and ^{15}O water [40]. Comparison of ^{82}Rb -PET images with $^{99\text{m}}\text{Tc}$ -Tetrofosmin images obtained with SPECT-CZT scanner is shown in Fig. 16.7.

^{18}F -Flurpiridaz (BMS-747158-02, Lantheus Medical, Inc.) is a novel PET mitochondrial complex-1 inhibitor indicated for detection of CAD and risk stratification. Flurpiridaz is an analog of

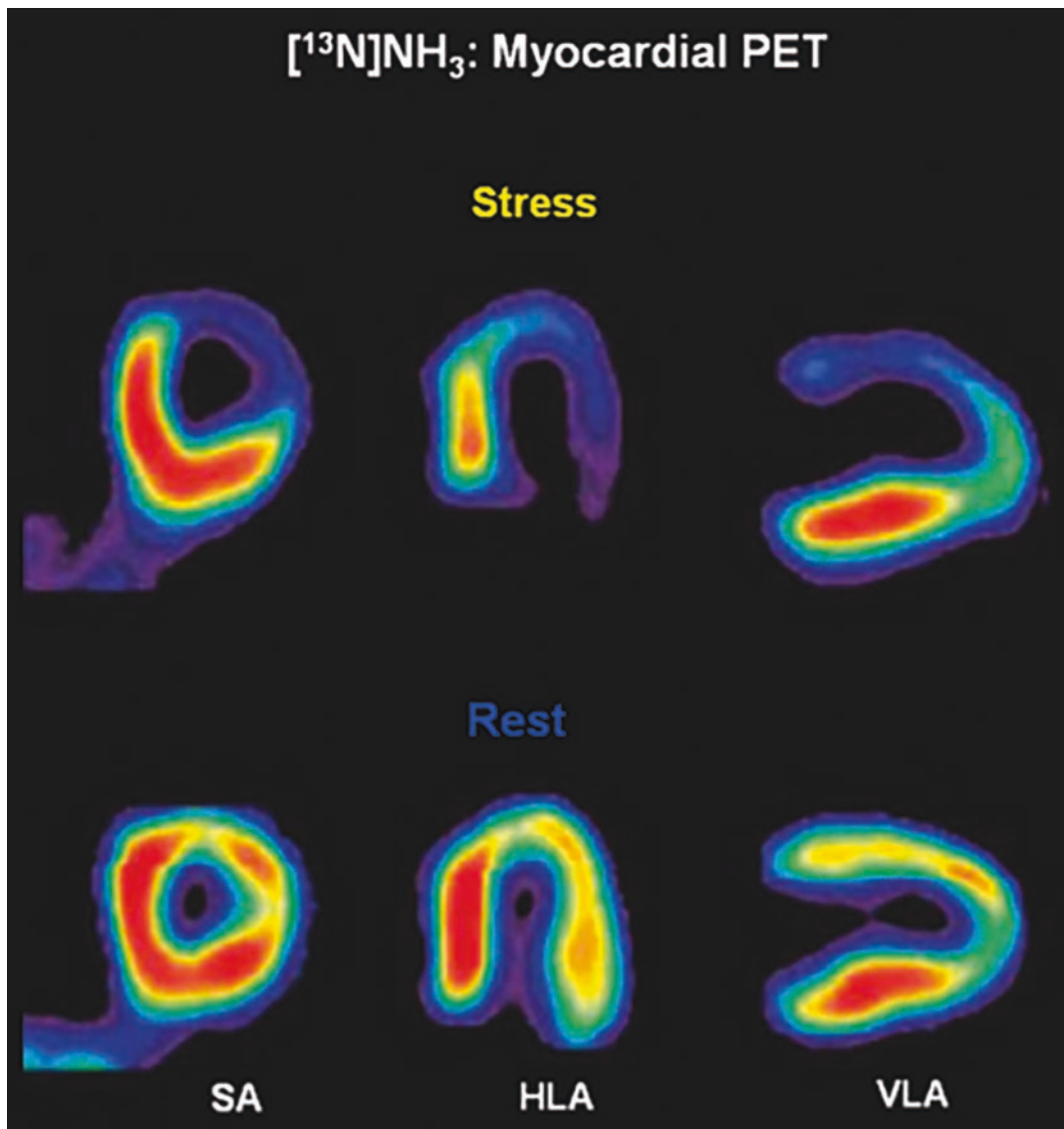


Fig. 16.6 Myocardial blood flow imaging with $[^{13}\text{N}]\text{NH}_3$ ammonia-PET demonstrating anterior and lateral defects during pharmacological stress and significant improve-

ment at rest, consistent with ischemia. SA short axis, HLA horizontal long axis, VLA vertical long axis [39]

mitochondrial complex-1 (MC1) inhibitor that specifically binds to the MC1 receptors on the inner mitochondrial membrane. Structurally it is an analog of the known MC-1 inhibitor, pyridaben. $[^{18}\text{F}]\text{Flurpiridaz}$ can provide improved image quality due to the shorter positron range and longer half-life, enabling delayed imaging post injection. The longer half-life of ^{18}F also provides an opportunity for exercise stress protocols.

The superior pharmacokinetic profile of $[^{18}\text{F}]\text{Flurpiridaz}$, including its sustained myocardial extraction at high flow rates (Fig. 16.5), enables the possibility of enhanced assessment of absolute quantification of myocardial flow reserve to better identify multivessel disease, microvascular disease, and response to treatment of endothelial dysfunction [41]. $[^{18}\text{F}]\text{Flurpiridaz}$ was evaluated in an initial Phase III trial with mixed results and

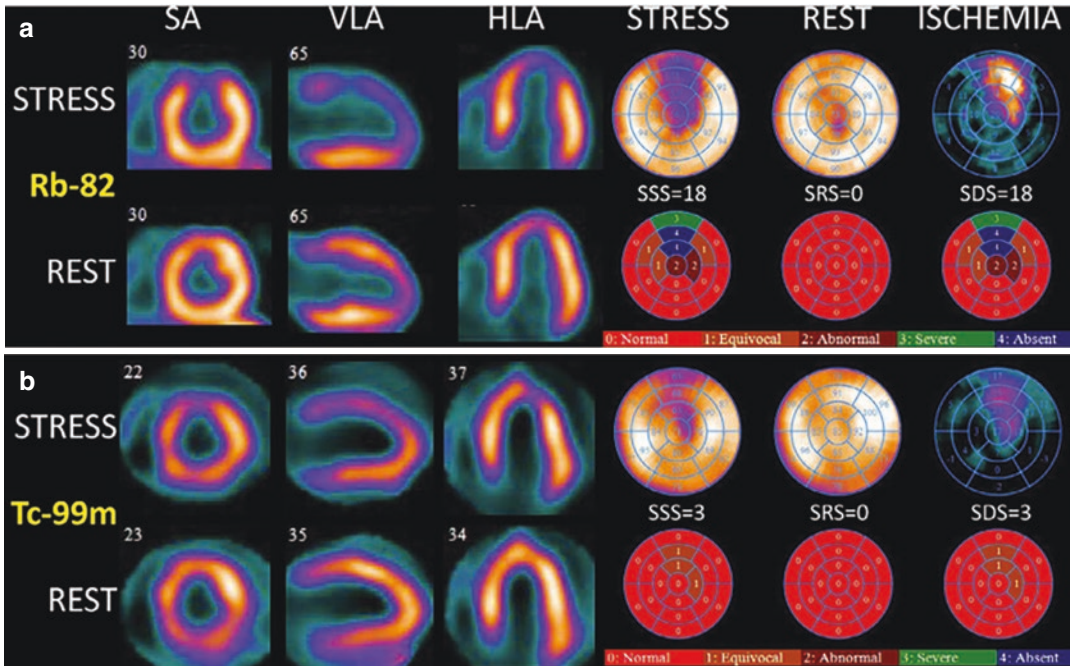


Fig. 16.7 ^{82}Rb -PET/CT (a) and ^{99m}Tc -Tetrofosmin SPECT-CZT (b) images in a 52-year-old man 3 months following PCI of the LAD coronary artery. Persantine ^{82}Rb -PET images demonstrate substantial residual ischemia in the LAD territory with sum stress and sum defect

scores (SSS and SDS respectively) equal to 18 (26% of LV). Exercise ^{99m}Tc -SPECT images in the same patient showed milder ischemia with SSS = SDS = 3 (4% of LV) due to lower tracer retention and lower hyperemic stress compared to persantine ^{82}Rb PET. (From [2])

is currently undergoing a second Phase III trial sponsored by GE Healthcare [2].

16.3.2 Myocardial Metabolism

Understanding the myocardial metabolism of substrates is very important for understanding the pathophysiology of various cardiac diseases and for designing therapeutic interventions. The heart requires a constant supply of energy to sustain contractile function. The energy is supplied by hydrolysis of ATP, which is primarily derived from the aerobic metabolism. The myocardium chooses between various substrates, such as free fatty acids (FFA), glucose, lactate, and ketone bodies (Fig. 16.8) [42]. The tricarboxylic acid (TCA) cycle is linked to the myocardial oxygen consumption via the electron transport chains, which supply most of the energy in the form of ATP. The amount of oxygen required, however, depends on the substrate. For example, one mol-

ecule of glucose requires 12 oxygen atoms to produce 38 ATP molecules. In contrast, one molecule of palmitate requires 46 oxygen atoms to produce 130 molecules of ATP. The selection of an appropriate substrate, however, depends on several conditions, such as plasma concentration of the substrate, hormonal control (insulin, glucagon, and catecholamines levels), stress, and physical activity.

In the normal myocardium, and also with moderate levels of exercise, FFAs are considered the preferred substrate for metabolism at rest. In the fasting state, FFA levels in circulation are high and insulin levels are low so that up to 80% of energy is derived from the FFA metabolism. A diet rich in carbohydrates increases the plasma glucose and insulin levels, and then glucose becomes the preferred substrate [43, 44]. With strenuous exercise, the release of lactate into the circulation from skeletal muscle increases and lactate will then become the major fuel for myocardial metabolism.

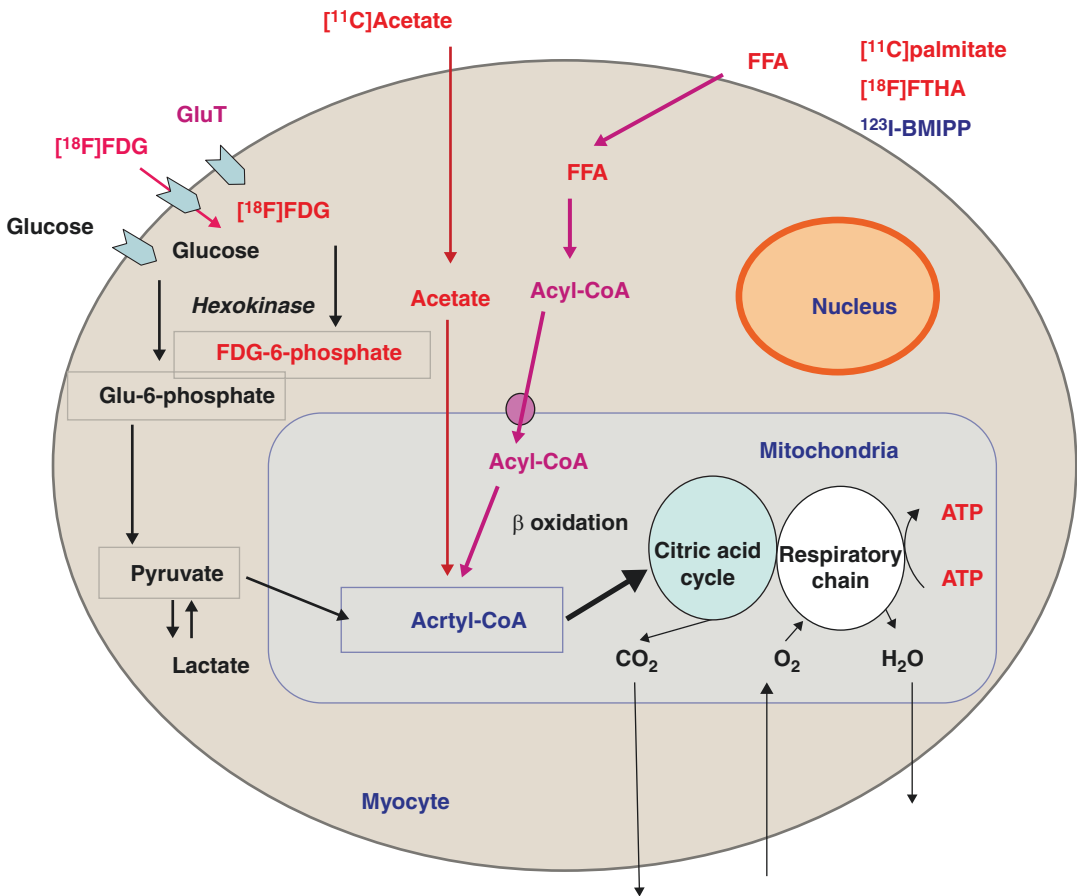


Fig. 16.8 PET and SPECT radiotracers to image myocardial substrate utilization and metabolism

In various pathological conditions, the myocardial metabolism can be changed significantly. In ischemic myocardium, the oxidative metabolism is reduced and as a result, there is a shift from an aerobic to an anaerobic metabolism. With the lack of a sufficient oxygen supply, glucose is now metabolized to lactate (glycolysis). With ischemia, glucose is the preferred substrate regardless of the availability of other fuels [44, 45]. For ischemic heart disease, the major player in the disease pathophysiology is the reduction in regional or focal perfusion. Changes in regional metabolism are a consequence of reduced blood flow to these areas.

Changes in myocardial metabolism may also play a key role in various other cardiac conditions, such as heart failure, cardiomyopathy, and diabetes, which involve the myocardium more globally, and involve the myocardium as a whole.

However, due to difficulties in evaluating metabolism in human subjects, the alterations in the myocardial metabolism under such conditions are poorly understood [46]. The substrate utilization may vary depending on the extent of CAD and prior drug therapy to improve LV function. For example, long-term treatment with a β -adrenergic receptor antagonist was reported to be associated with a switch in myocardial metabolism away from FFA oxidation towards glucose metabolism [47]. Studies in animal models of diabetes mellitus have demonstrated an upregulation of myocardial fatty acid utilization and a reduction of the insulin-mediated glucose transport. However, little is known about the effect of diabetes mellitus on the human heart.

In the era of traditional SPECT, MPI alone and exercise testing, with relatively long-lived tracers that are retained by the myocardium were

advantageous but, with the shift to more sensitive imaging devices (i.e., PET and cardiac-dedicated SPECT), MBF quantification and an emphasis on dose reduction, short-lived tracers offer more advantages.

16.3.2.1 Glucose Metabolism

Glucose is transported into the myocardial cell by facilitated diffusion of insulin-independent GLUT 1 and insulin-dependent GLUT 4 glucose transporters [48]. Intracellularly, glucose is rapidly phosphorylated to glucose 6-phosphate, which is further metabolized (glycolysis) to pyruvate. Under aerobic conditions, pyruvate is converted to acetyl-CoA, which enters the TCA cycle in the mitochondria for oxidative metabolism (Fig. 16.8). Under anaerobic conditions, pyruvate is further metabolized to lactic acid.

[^{18}F]FDG that enters the myocardium is phosphorylated to FDG-6-phosphate but, then, does not enter further metabolic pathways; instead, it accumulates in the myocardium. Thus, the myocardial uptake of FDG reflects the uptake and metabolism of glucose [49, 50]. FDG-PET images reflect the relative distribution of FDG uptake in different regions of the myocardium. Also, the metabolic rate (MR_{glc}) of glucose in absolute units can be measured with PET based on dynamic imaging studies, mathematical modeling, compartment model analysis, or graphical plot analysis. Since the rate of the glucose uptake and FDG uptake is not equal, a lumped constant (LC) was developed to convert the FDG uptake to glucose uptake. Usually, the value of LC is fixed, and is approximately 0.6–0.7 for the FDG-PET measurement of MR_{glc} [51]. The LC, however, can vary over a wide range, depending on blood insulin levels and cardiac disease [52].

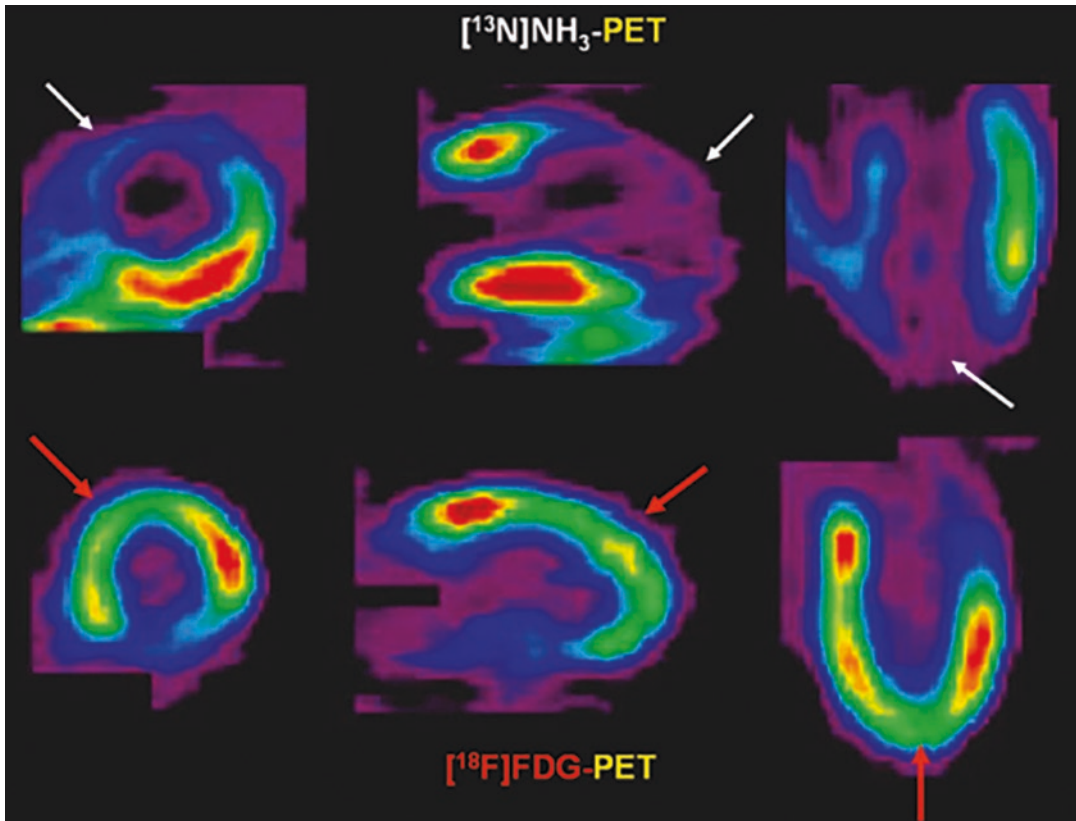


Fig. 16.9 FDG-PET to image myocardial viability. Classic mismatch showing FDG uptake in the areas of decreased myocardial perfusion identified by [^{13}N]NH₃

Detection of viability in ischemic heart disease is one of the most important aspects of the diagnostic and prognostic workup in patients with CAD. In some cases of hibernating myocardium, the resting flow based on PET or SPECT tracers cannot differentiate hibernating myocardium from irreversible myocardial scar formation. Relatively higher FDG uptake in an area of decreased myocardial blood flow in the dysfunctional myocardium, known as “flow metabolism mismatch,” indicates viable myocardium [53]. As a result, FDG-PET is considered as one of the gold standards for the determination of myocardial viability (Fig. 16.9).

16.3.2.2 Fatty Acid Metabolism

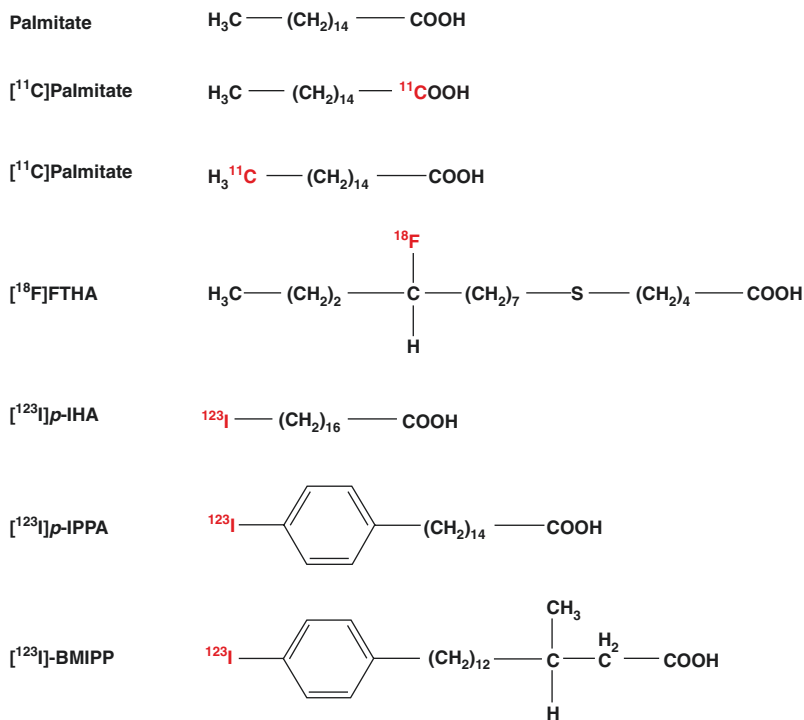
Since the FFAs are hydrophobic, they are delivered to the heart by binding to plasma proteins, albumin, or lipoproteins. After dissociating from proteins, FFAs easily pass through the myocardial membrane by diffusion or a facilitated transport mechanism. Based on clinical and animal experiments, it has been shown that CD36 plays a cru-

cial role in the fatty acid transport into the cells [54, 55]. Intracellularly, FFAs are activated as acylcoenzyme A (Acyl CoA) and then carried into the mitochondria through an acyl carnitine carrier system and catabolized by β -oxidation into two-carbon fragments, acetyl-CoAs, which enter the TCA cycle for further oxidative metabolism (Fig. 16.8). A part of FFAs is not oxidized but, is formed into triglycerides and myocardial structural lipids and stays in the myocardium for a long time. The straight-chain FFAs are generally metabolized through β -oxidation and released from the myocardium, while the development of modified FFAs is based on the concept of myocardial retention from metabolic trapping [56].

Radiolabeled Fatty Acids for PET

A physiological radiotracer 1- ^{11}C palmitate (Fig. 16.10) was the first FFA introduced to image fatty acid metabolism of the heart [57]. Subsequently, 14(*RS*)- ^{18}F fluoro-6-thiaheptadecanoic acid (FTHA) was developed as a metabolically trapped radiotracer [58].

Fig. 16.10 PET and SPECT radiotracers of free fatty acid analogs to assess myocardial metabolism



[¹¹C]Palmitate is biologically identical to non-radioactive circulating palmitate. The first-pass extraction fraction (0.67) is relatively high and the initial uptake, and regional distribution in the myocardium are largely determined by MBF [34]. It clears from the myocardium in a biexponential fashion. Once the tracer is taken up into the myocardium, β -oxidation breaks it down to generate acetyl-CoA. This [¹¹C] acetyl-CoA is oxidized via the citric acid cycle and finally released from the myocardium in the form of [¹¹C]CO₂. The rapid clearance fraction corresponds to β -oxidation, whereas the slow-washout fraction reflects the turnover rate of the intracellular lipid pool and is an index of FFA metabolism [56]. In severely ischemic myocardium, the regional uptake of [¹¹C]palmitate is reduced. The PET images provide a qualitative and semiquantitative evaluation of fatty acid metabolism. The quantitative value of myocardial fatty acid use and oxidation is difficult to estimate in absolute units (milliequivalents of free fatty acid per minute per gram of myocardium). Since the C-1 label of 1-[¹¹C]palmitate is removed in the initial step of β -oxidation, ω -[¹¹C]palmitate was proposed as a potential tracer to prolong the myocardial retention of trapped metabolites [59].

With FTHA, the rate of metabolic trapping is thought to be proportional to the rate of β -oxidation. In patients with CAD, estimates of myocardial FFA utilization (MFAU) in a normal myocardium were found to be approximately $5.8 \pm 1.7 \mu\text{mol } 100 \text{ g}^{-1} \text{ min}^{-1}$, while in patients with CHF, the MFAU was found to be elevated ($19.3 \pm 2.3 \mu\text{mol } 100 \text{ g}^{-1} \text{ min}^{-1}$) [34, 60]. Further, because FTHA does not trace the FFA uptake under hypoxic conditions accurately, several ¹⁸F analogs have been developed. It is still not clear which tracer is the most reliable or the most clinically useful PET tracer to image fatty acid metabolism in different cardiac diseases [46].

Radiolabeled Fatty Acids for SPECT

Since the 1970s several iodinated fatty acid tracers for SPECT have been developed (Fig. 16.10) by introducing radioiodine to the terminal position of fatty acids without significant alteration of the extraction efficiency, compared with the

natural FFAs [55, 56, 61]. The two groups of iodinated fatty acid compounds include straight-chain FFAs and modified branched FFAs. In a clinical study, ¹²³I-16-iodoheptadecanoic acid (IHA), an analog of stearic acid demonstrated a high-quality image early after injection but, the image quality deteriorated rapidly because of the rapid reduction of myocardial counts and increase in background counts due to deiodinated radioiodine [62]. To prevent in vivo deiodination, the phenyl fatty acids were developed by attaching iodide to the para or ortho position of the phenyl ring (IPPA). For routine clinical use, however, the rate of metabolism and clearance of IPPA is still relatively too fast for SPECT imaging studies.

In order to develop a tracer with more prolonged cardiac retention and with improved image quality, a methyl branching was introduced at the β -carbon position to slow the myocardial clearance by inhibiting β -oxidation. Two iodinated branched fatty acid analogs, 15-(*p*-iodophenyl)-3-*R,S*-methylpentadecanoic acid (BMIPP) and 15-(*p*-iodophenyl)-3,3-methylpentadecanoic acid (DMIPP) were, therefore, developed [55, 56, 63, 64]. FTHA has shown to be metabolically retained in the myocardium and has very good imaging properties in normal human subjects, and in patients with CAD. The concept underlying BMIPP imaging is metabolic trapping of BMIPP-CoA, similar to FDG, but by inhibition of β -oxidation through the introduction of methyl branching, at the β -carbon position. Under the condition of ischemia, a reduction in BMIPP uptake is observed, reflecting the reduction in ATP production due to depressed oxidative fatty acid metabolism and substrate shift from fatty acids to glucose (Fig. 16.11). When compared with myocardial perfusion imaging, BMIPP imaging enables “ischemic memory imaging,” with detection of previous myocardial ischemia (metabolically stunned myocardium) and viable but chronically dysfunctional myocardium (hibernating myocardium) [55]. Also, in cardiomyopathy, BMIPP imaging may be useful for the early detection of HCM, the differentiation of ischemic cardiomyopathy from idiopathic DCM, and also for the

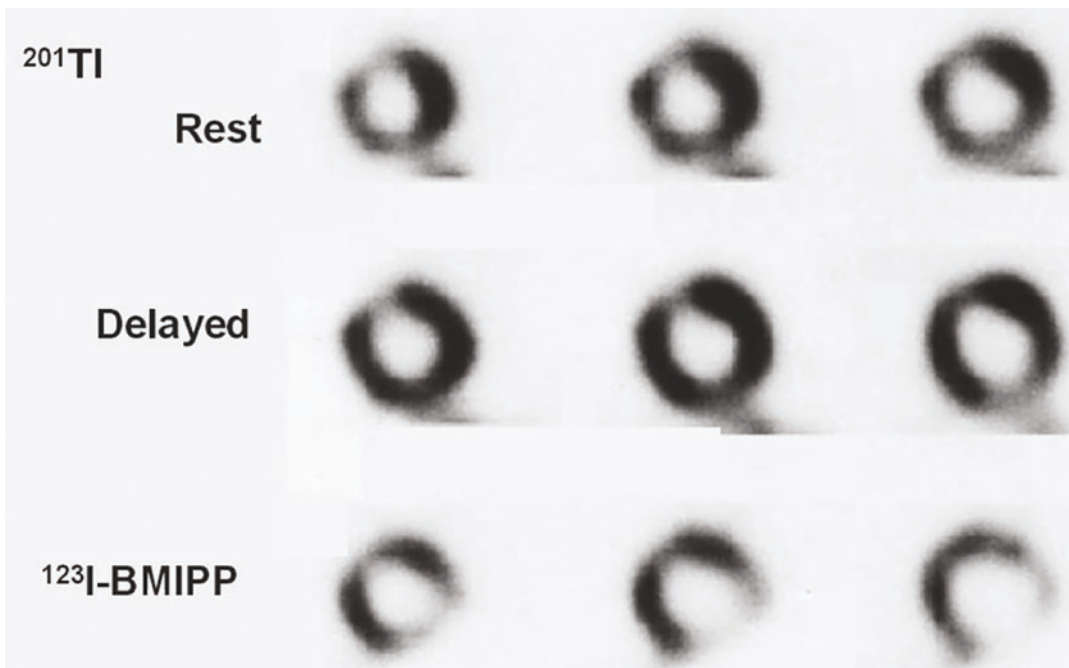


Fig. 16.11 Myocardial metabolic imaging using ^{123}I -BMIPP in patients with unstable angina: Although ^{201}Tl scans did not show definite perfusion abnormalities,

decreased BMIPP uptake was noted in the lateral region, indicating decreased regional myocardial fatty acid metabolism [56]

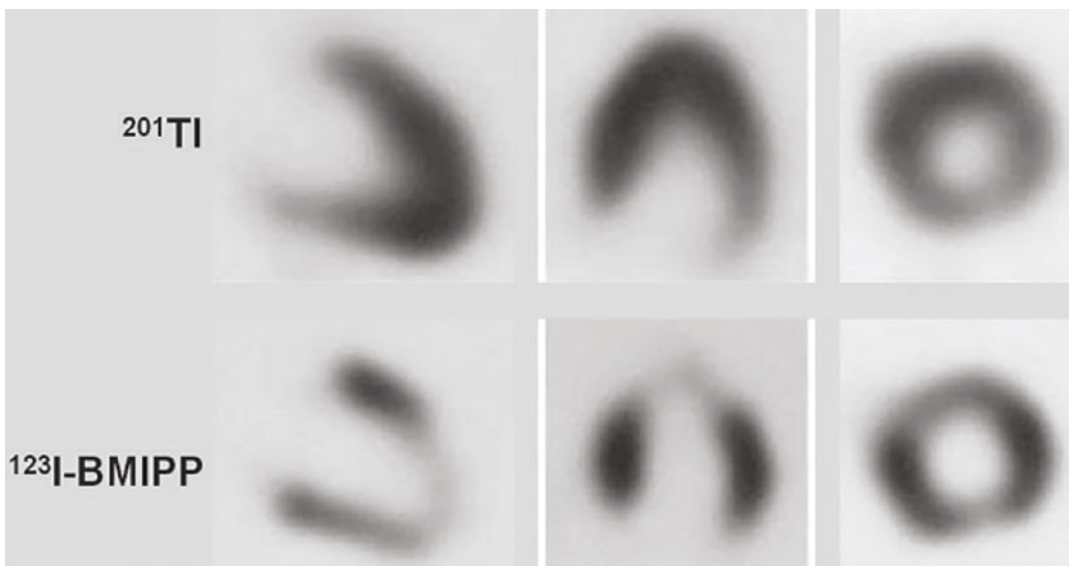


Fig. 16.12 Myocardial metabolic imaging using ^{123}I -BMIPP in patients with hypertrophic cardiomyopathy (HCM). There is increased ^{201}Tl uptake in the apex to the antero-septal wall but, BMIPP uptake is reduced in that

area. Discordant BMIPP uptake less than blood flow in the hypertrophic area is a rather early phenomenon of HCM [55]

prediction of prognosis (Fig. 16.12). ^{123}I -BMIPP has been the most commonly used commercially available SPECT tracer to assess fatty acid metabolism in patients, especially in some of the European countries and in Japan.

16.3.2.3 Oxidative Metabolism

The assessment of myocardial oxidative metabolism involves the estimation of myocardial ventricular oxygen consumption (MVO_2) in absolute units, $\text{mL min}^{-1} \text{g}^{-1}$. Under steady-state conditions, MVO_2 provides an accurate measure of overall myocardial metabolism regardless of which substrate or fuel is used. Based on the determination of myocardial blood flow, using ^{15}O water, myocardial blood volume using ^{15}O CO, and oxygen inhalation studies using ^{15}O O₂, myocardial oxygen extraction can be determined. The MVO_2 is then estimated using the plasma oxygen content as the arterial input function. In normal subjects, an average MVO_2 is $0.097 \pm 0.022 \text{ mL min}^{-1} \text{g}^{-1}$ [65]. While this method provides an absolute quantitative estimation of regional MVO_2 in various cardiac diseases, the PET imaging studies involving ^{15}O ($T_{1/2} = 2 \text{ min}$) are not practical for routine clinical use.

^{11}C Acetate

Acetate is avidly extracted from the coronary circulation and rapidly distributed in the myocardium. In cytosol, it is activated to acetyl-CoA and, subsequently, enters the TCA cycle in the mitochondria for oxidation and metabolism to ^{11}C O₂ and water (Fig. 16.8). It is important to realize that the myocardial kinetics of ^{11}C acetate is independent of the metabolic milieu, such as the blood glucose level or FFA concentration in the blood [66]. Following intravenous bolus administration, the myocardial washout of activity demonstrates a biexponential clearance. The myocardial oxidative metabolism, however, can be estimated based on the rapid washout rate determined, using monoexponential curve fitting of the time–activity data [67]. Because of its high myocardial first-pass extraction fraction, the early phase (1–3 min) is flow-dependent and provides an estimation of regional myocardial perfusion [68]. With ^{11}C acetate, simultaneous

determination of myocardial blood flow and oxygen consumption can be performed with a single data acquisition [46].

16.3.3 Myocardial Presynaptic Adrenergic Neuronal Imaging

The cardiac sympathetic nervous system remains of interest for molecular imaging, due to the direct relationship between sympathetic activity, cardiomyocyte β -adrenoceptor expression, and ventricle remodeling. In the failing heart, increased sympathetic drive leads to increased norepinephrine stimulation and downregulation of adrenoceptors, the pathophysiology underlying the common use of β -blocker therapy to normalize contractility [69].

The mammalian heart is characterized by dense adrenergic innervation with a norepinephrine (NE) concentration gradient from the atria to the base of the heart and from the base to the apex of the ventricles. In contrast, parasympathetic innervation is distributed throughout the atrial and ventricular walls, with a gradient from the former to the latter, with acetylcholine (ACh) being the main neurotransmitter. Both, the sympathetic and parasympathetic tones control the rate of the physiologic stimulation and conduction, while the contractile performance is primarily modulated by sympathetic neurotransmission. The major neurotransmitters of the sympathetic and parasympathetic systems, NE and ACh, define the stimulatory and inhibitory physiologic effects of each system.

The NE is produced from tyrosine within a neuron (Fig. 16.13). Tyrosine is converted to DOPA, which is converted to dopamine by *DOPA decarboxylase*. Dopamine is then transported by a vesicular monoamine transporter (VMAT2) into the vesicles, where it is converted to NE by dopamine β -hydroxylase. Adrenergic nerve stimulation leads to the release of NE into the synapse. The sympathetic neurotransmission in the heart is mediated by adrenoceptors of type β_1 and β_2 , which are located on the myocardial cells. Only a small amount of NE, released into the

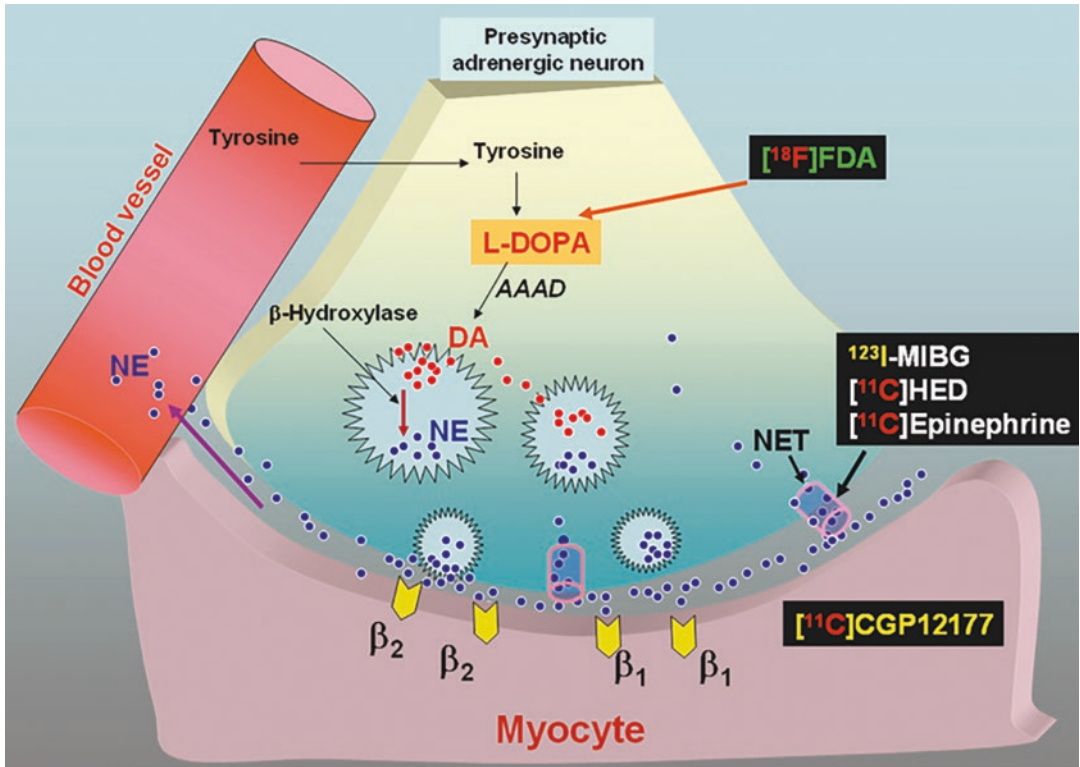


Fig. 16.13 Adrenergic neurotransmission in the heart. PET and SPECT tracers for imaging presynaptic adrenergic neurons and postsynaptic adrenoceptor density

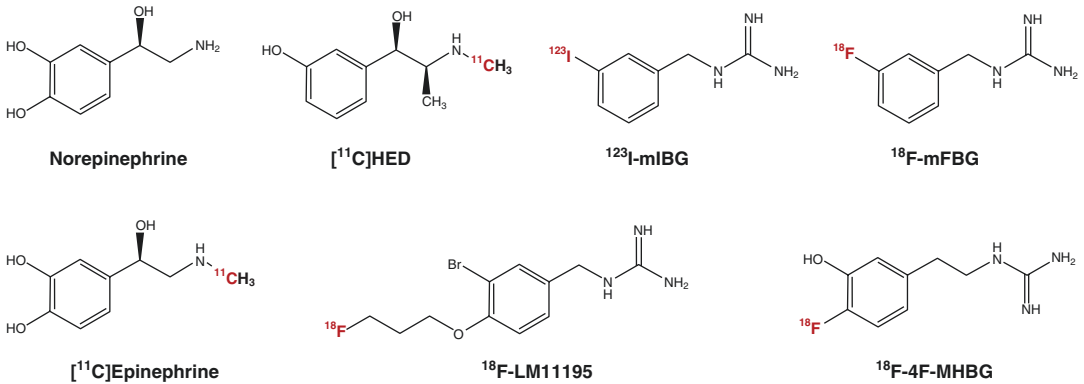


Fig. 16.14 Norepinephrine analogs labeled for PET and SPECT imaging studies to assess cardiac neurotransmission

synapse, binds to the adrenoreceptors while most of the NE in the synapse undergoes reuptake (uptake-1 mechanism) back into the presynaptic nerve terminal by a saturable and Na⁺, temperature, and energy-dependent mechanism (uptake-1) via a neuronal norepinephrine transporter (NET) or by nonsaturable, and not Na⁺, temperature, or energy dependent mechanism (uptake-2). The free cytosolic NE is degraded by MAO to dihydroxyphenylglycol (DHPG).

16.3.3.1 Radiotracers for Presynaptic Sympathetic Innervation

All of the radiotracers developed for imaging cardiac sympathetic innervation are analogs of NE (Fig. 16.14). As discussed earlier, NE within the synapse is transported back into the presynaptic neuron terminals via NETs, based on the uptake-1 mechanism. Structural analogs of NE are also transported into synaptic terminals by this uptake-1 mechanism [70].

[¹¹C]Hydroxyephedrine (HED)

PET radiotracers (Fig. 16.14) resemble the endogenous NE more closely than ¹²³I-MIBG. Two different groups of PET tracers are available for presynaptic sympathetic imaging of the heart; radiolabeled catecholamines and radiolabeled catecholamine analogs [71, 72].

[¹¹C]Hydroxyephedrine (HED) is the most widely used tracer for cardiac neuronal imaging. HED has a high affinity for the NETs and shows negligible non-specific binding. Following the transport into the presynaptic terminal, it is not metabolized by MAO or COMT enzymes [71, 73]. Since HED is not metabolized, it diffuses out of the nerve terminal and is transported back into the nerve terminal. Therefore, HED myocardial retention is actually dependent on both the continuous release and reuptake by NETs [72].

While HED is a false neurotransmitter, [¹¹C] epinephrine (EPI) is a more physiological tracer since it is primarily a circulating hormone produced together with NE by the adrenal medulla and other chromaffin tissues. Unlike HED, EPI is degraded by MAO but, its storage in the vesicles

is very efficient, preventing it from degradation and causing slow clearance of the tracer from the heart. Therefore, EPI reflects the whole cascade of uptake, metabolism, and storage of neurotransmission, while the primary target for HED and MIBG is the uptake-1 system. Both, HED and EPI can be synthesized with high chemical purity (>95%) and SA (33–74 GBq μmol⁻¹).

¹²³I-MIBG

Guanethidine is a potent neuron-blocking agent that acts selectively on sympathetic nerve endings. Based on this molecule, ¹³¹I-*meta*-iodobenzylguanidine (MIBG) was initially developed as an agent for imaging tumors of adrenal medulla origin [74]. The avid heart uptake and retention of MIBG observed in animal biodistribution studies strongly suggested that MIBG might also be successfully used for imaging cardiac sympathetic neurons [75]. Consequently, ¹²³I-MIBG was developed for imaging the heart, in patient studies [76]. MIBG is transported into presynaptic terminals by the uptake-1 mechanism and is stored mainly in the NE storage vesicles. In other words, MIBG and NE have the same mechanisms for uptake, storage, and release. Unlike NE, MIBG does not bind to receptors on the myocardial cell membrane, and does not undergo any metabolism within the presynaptic terminals [71, 77]. As a result, MIBG is retained in sympathetic nerve endings, and provides clinically useful diagnostic information for different cardiac diseases.

For practical clinical application, the SA and radio-chemical purity of MIBG are critical factors. The unlabeled catecholamines (cold MIBG) may compete with the labeled tracer and may not only limit image quality but, also, cause pharmacologic action via adrenoceptor activation. The specific activity (SA) of commercial preparation of ¹²³I-MIBG (Adreview) is ~1.0 GBq/mg and is sub-optimal for imaging studies. Therefore, high SA ¹²³I-MIBG (>50 GBq) may be beneficial for clinical studies.

To overcome the limitations of [¹¹C]HED and ¹²³I-MIBG, several ¹⁸F-labeled MIBG analogs

have been developed [78–81]. ^{18}F -*N*-[3-bromo-4-(3-fluoro-propoxy)-benzyl]-guanidine (^{18}F -LMI1195) showed specific uptake in the heart as assessed by in vivo PET imaging in rabbits. Stable retention under a desipramine chase indicates promising properties as a new class of PET tracer for visualizing the cardiac nervous system, mimicking physiologic norepinephrine turnover at nerve terminals [79]. In a phase I clinical study, [^{18}F]4F-MHPG and [^{18}F]3F-PHPG have demonstrated that both tracers provide high-quality cardiac PET images, with extremely low uptake in lungs and acceptable uptake levels in the liver. Comparing the two tracers, an advantage of [^{18}F]4F-MHPG is its more rapid clearance from the liver [78].

16.3.3.2 Radiotracers for Cardiac Neuroreceptors

The sympathetic adrenoreceptors β_1 and β_2 , located on the myocardial cells, play a major role in the regulation of cardiac function. In the healthy myocardium, β_1 -receptors are the most abundant, forming 80% of all β -receptors, while in heart failure the proportion of β_2 -adrenoceptors may increase to 50% [72, 82]. Also, sympathetic activation results in the elevation of systemic catecholamine levels and subsequent downregulation of β -receptors. Many different pharmaceuticals, that act as cardiac receptor antagonists, such as β -blockers or β -receptor antagonists, are used in cardiological practice. The efficacy of these drugs depends on many different factors, especially the β -receptor density. Noninvasive imaging and quantitation of β -receptor density (B_{\max}) before initiation of therapy with β -blockers might predict the outcome of therapy.

[^{11}C]CGP-12177 (4-(3-*t*-butylamino-2-hydroxypropoxy)-benzimidazol-1), a hydrophilic, nonselective antagonist, that binds to the β -receptors with high affinity (0.3 nmol L^{-1}), was one of the first ligands developed for cardiac PET adrenoreceptor imaging studies [83]. So far, [^{11}C]CGP-12167, is the only tracer, that has been used more extensively in patient populations, such as patients with dilated hypertrophic and arrhythmogenic right ventricular cardiomyopathy [71,

72]. Because of the difficulties involved in the synthesis of this tracer, the *N*-isopropyl derivative, [^{11}C]CGP-12388 was developed as an alternative for clinical use [84].

16.3.3.3 Clinical Applications

Sympathetic nerve endings are easily damaged by ischemia, in comparison to myocardial cells, and sympathetic function disorders are known to persist for a certain period even after alleviation of the ischemia. The utility of cardiac sympathetic imaging is most widely studied in patients who have heart failure with reduced ejection fraction (HFrEF) [6, 85, 86] (Fig. 16.15).

PET imaging of the cardiac autonomic nervous system has advanced in recent years and multiple pre- and postsynaptic tracers have been used to determine the involvement of the sympathetic dysinnervation at different stages of heart diseases, such as ischemia, heart failure, and arrhythmia. In general, [^{11}C]HED is the most widely used PET tracer for cardiac neuronal imaging. In a healthy heart, there is an even distribution of HED over the left ventricle, making it a valuable tracer for detecting specific regional defects of the presynaptic sympathetic system in disease [72]. In patients with dilated cardiomyopathy there is a loss of neurons or downregulation of uptake-1. In a patient with idiopathic dilated cardiomyopathy and severely reduced left ventricular ejection, the myocardial retention of HED was reduced significantly (Fig. 16.16). In heart failure patients, the extent of denervation denoted by HED retention predicts sudden cardiac arrest [87, 88]. The [^{11}C]HED is the most commonly used PET tracer for sympathetic nerve imaging. The superior sensitivity and quantitative capability of HED-PET allow for reliable assessment of regional neurohumoral abnormalities.

In patients with unstable angina, MIBG-SPECT makes it possible to identify the culprit coronary artery with a high probability and, thus, is of diagnostic value (Fig. 16.16). In patients with heart failure, the increased washout rate and the decreased heart/myocardium (H/M ratio) on the delayed MIBG image become marked with an increase in hypofunction in the left ventricle, regardless of the underlying diseases [89].

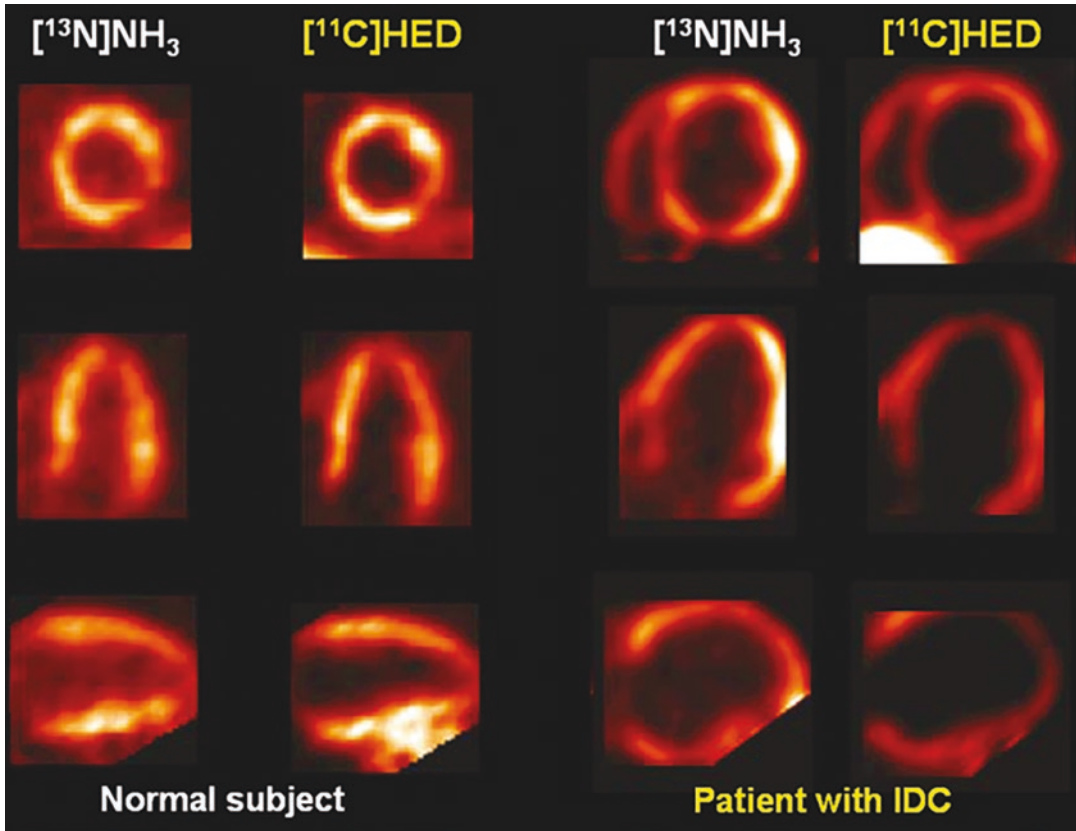


Fig. 16.15 $[^{11}\text{C}]\text{HED}$ -PET for imaging presynaptic sympathetic innervation in the heart. In a normal subject, there is an even distribution of HED in the heart similar to the myocardial perfusion images of $[^{13}\text{N}]\text{ammonia}$ -PET. In a

patient with idiopathic dilated cardiomyopathy (IDC) and severely reduced left ventricular ejection fraction (22%), there is a significantly reduced retention of HED compared with the myocardial perfusion [72]

Similar results have been reported from studies on dilated cardiomyopathy, hypertrophic cardiomyopathy (HCM), valvular heart disease, pulmonary hypertension, amyloidosis, and diabetes [77]. ^{123}I -MIBG planar/SPECT has been used in numerous studies to document regional denervation for arrhythmic event risk assessment [90].

16.3.4 Cardiac Sarcoidosis (CS)

As discussed earlier, CS occurs most commonly in patients who are 20–40 years old, with a predominance of female patients. The cardiovascular system is the third most common site of sarcoidosis and is involved in 25–50% of patients. Patients with heart failure have a particularly

poor prognosis. Because corticosteroid therapy improves cardiac function and prognosis, accurate diagnosis, and timely intervention for improving outcomes is necessary [25, 91].

In the 1990s, it was documented that a combination of ^{201}Tl chloride and ^{67}Ga citrate scintigraphy may be useful not only in the diagnosis of cardiac sarcoidosis but, also, in the prediction of the effects of corticosteroids [92]. ^{67}Ga -SPECT/CT scanning was also shown to be a very useful diagnostic imaging technique because it improves the diagnostic specificity of ^{67}Ga -SPECT to allow the highly specific diagnosis of cardiac sarcoidosis [93].

It is well recognized that glucose metabolism is increased in inflammatory cells. Macrophages and CD4+ T cells present in sarcoid granulomas have a high energy demand requiring increased

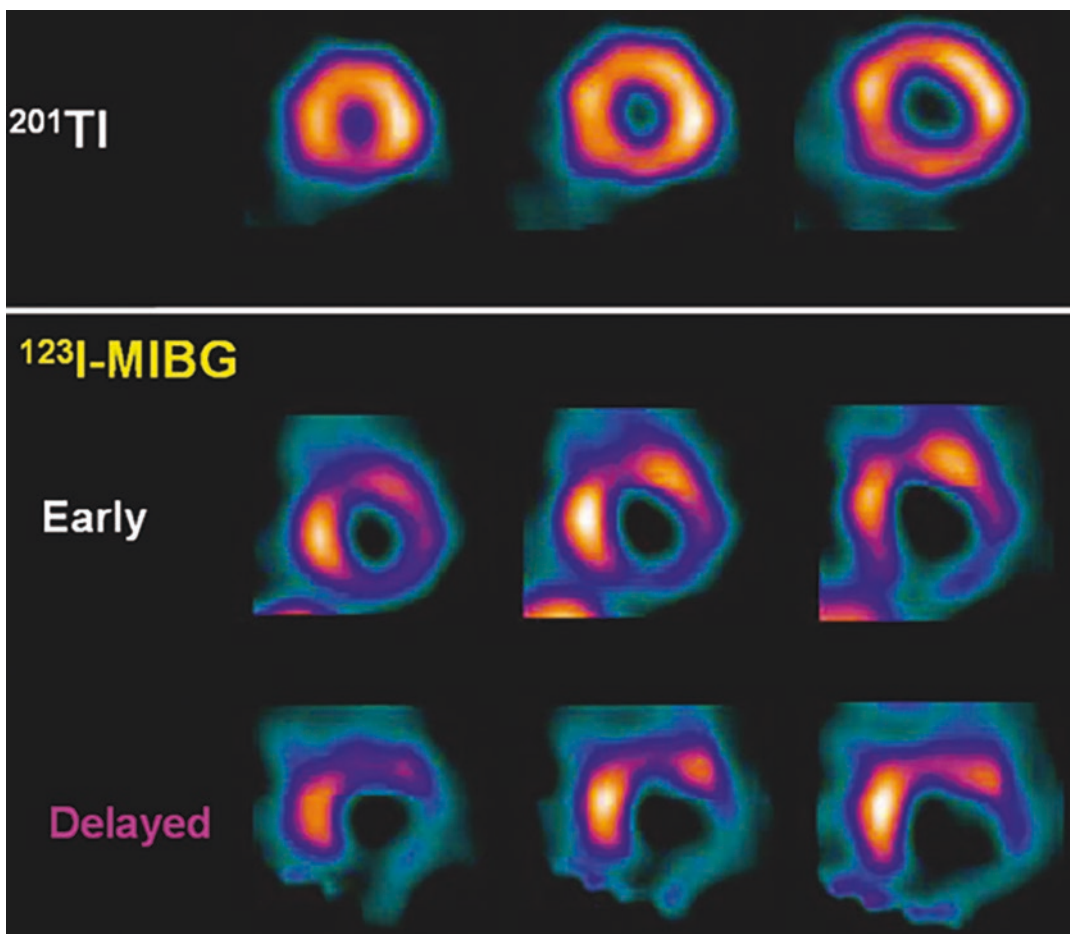


Fig. 16.16 ^{123}I -MIBG imaging in patient with ischemic heart disease. In a patient with unstable angina, myocardial perfusion with ^{201}Tl -SPECT at rest was relatively normal with no significant findings. In contrast, MIBG

SPECT (early and delayed) showed decreased accumulation in the infero-posterior wall. Coronary angiography performed later, and advanced stenosis was recognized in the proximal part of the RCA [77]

glycolysis and, therefore, cellular inflammation can be detected by PET/CT using [^{18}F] FDG. Consequently, the clinical utility of FDG PET/CT for diagnosis and management in patients with known or suspected CS was investigated. Background cardiomyocyte uptake, however, represents a major limitation of FDG-PET scan, and may be suppressed by fasting, fatty meals, and heparin infusion, though nonspecific uptake may still be present in some patients [91].

FDG-PET is currently the best clinical tool for the assessment of myocardial inflammation in CS [25, 94]. Suppression of baseline myocardial FDG uptake via fasting and adoption of a very

low carbohydrate diet allows for visualization of FDG uptake by inflammatory cells. The optimal PET protocol used to evaluate CS requires rest myocardial perfusion, cardiac and whole body FDG-PET imaging. FDG-PET imaging provides a good diagnostic accuracy for CS. However, accurate interpretation may be hampered by physiologic accumulation of FDG in the myocardium, which is seen in up to 20% of patients even after elaborate preparation [94]. Most patients with cardiac sarcoidosis have extracardiac involvement, and identification of the extracardiac lesions is essential in diagnostic evaluation of patients with suspected CS. The major advantage

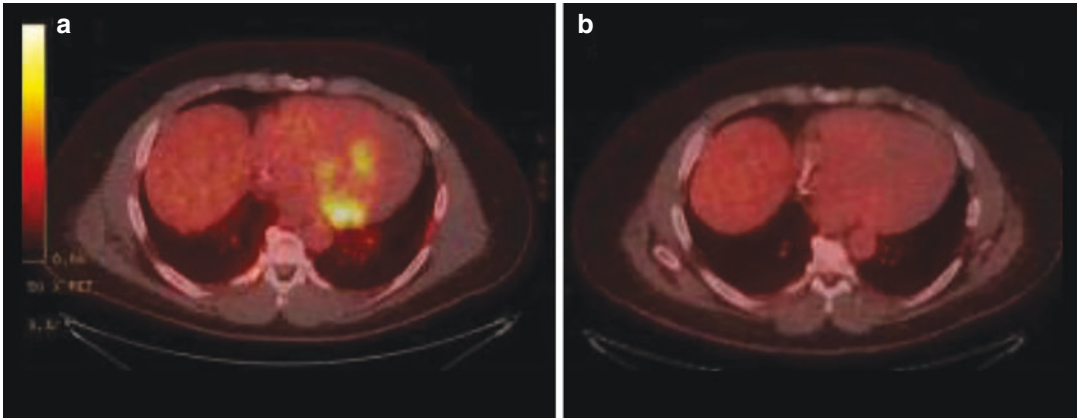


Fig. 16.17 Representative [^{18}F]FDG-PET images from a patient with cardiac and pulmonary sarcoidosis. Baseline cardiac FDG-PET images (Panel **a**) demonstrate a moderate-sized area of abnormal FDG uptake extending

to medial and basal segments of the inferior and inferoseptal wall. After treatment with prednisone and mycophenolate mofetil, there is resolution of cardiac FDG uptake (Panel **b**) [25]

of whole-body FDG PET/CT is that it enables evaluation of the systemic extent of sarcoidosis beyond the myocardium. Figure 16.17 shows the diagnostic value of FDG-PET in CS, and to monitor treatment response. The advantage of FDG-PET in the diagnosis of CS, the detection of the extracardiac sarcoidosis involvement, and the response to therapy is shown in Fig. 16.18.

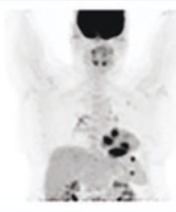





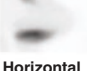

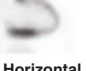
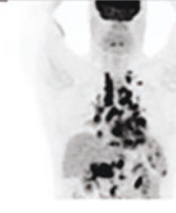




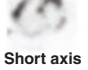



Radiotracers that do not have any uptake in the myocardium but, are taken up by inflammatory cells have also been evaluated for imaging CS. [^{18}F]Fluorothymidine (FLT), a tracer to study cellular proliferation and DNA synthesis has been reported to be useful for the detection of CS [91, 96]. The main advantage is that FLT PET/CT can provide detectability as high as that for FDG PET/CT but, without fasting or change in the diet. In CS lesions containing granulomas with high-turnover traits, proliferation tracers accumulate predominantly in active lesions. A correlation between FLT uptake and myocardial scarring was observed indicating that FLT-PET/CT allows detection of areas that are developing into myocardial scars [97].

Somatostatin receptors (SSTRs), specifically subtype 2, are expressed not only in neuroendocrine tumors (NETs) but, also, on the surface of activated inflammatory cells such as macrophages, epithelioid cells, and multinucleated giant cells, which are the main constituents of sarcoid granuloma [98]. SSTR-agonists such as [^{111}In]-DTPA-octreotide (Octreoscan) and [^{68}Ga] labeled Dotatoc, dotatate, and Dotanoc have shown potential clinical utility for detecting CS [99–102]. SSTR imaging has the potential for differentiation of active CS lesions from those in the chronic phase because fibrotic tissue, which is seen in the chronic phase, lacks extensive SSTR expression [91].

16.3.5 Cardiac Amyloidosis (CA)

CA is more prevalent than previously expected, contributing to significant cases of heart failure with preserved ejection fraction [103]. Recent developments in treatment strategies have also shown the importance of early and accurate diag-

Fig. 16.18 FDG-PET to assess response to therapy in cardiac sarcoidosis (CS). Examples of using ¹⁸F-FDG PET to assess response to therapy. (Top) Patient with no response to treatment. (Bottom) Patient with marked response of both extra CS and CS to treatment. (From [95])

		Baseline	After treatment
		No Response	Whole Body FDG 
	Myocardial Perfusion	 	 
	Inflammation (FDG)	 	 
		Baseline	After treatment
		Marked Response	Whole Body FDG 
	Myocardial Perfusion	 	 
	Inflammation (FDG)	 	 

nosis in CA. In patients with CA with amyloid fibril protein (AL-CA), novel antiplasma cell therapy has been proved effective, even in populations of patients with refractory disease. A lower mortality rate and improved overall survival can be achieved with earlier diagnosis of AL amyloidosis [42]. Introduction of therapy with the FDA-approved drug, tafamidis, which binds to transthyretin (TTR) and inhibits tetramer dissociation and amyloidogenesis, has improved outcomes in patients with ATTR-CA [26, 91]. The improved therapeutic options render accurate and early diagnosis critical.

Several ^{99m}Tc labeled bone-seeking SPECT radiopharmaceuticals (Fig. 16.19) have shown the clinical utility to detect and provide confirmatory diagnosis of CA. Additionally, PET techniques are emerging in amyloidosis [91, 104–108]. Although the role of the bone-seeking agent ¹⁸F-sodium fluoride for the workup of ATTR-CA is still under debate because of low signal intensity, PET amyloid markers (Fig. 16.19) originally developed for neurology to identify β-amyloid in neurodegenerative disease have also been used to detect cardiac amyloidosis.

A resurgence of interest and an improved understanding of the performance characteristics of CA imaging with SPECT using ^{99m}Tc -labeled bone-seeking tracers, such as PYP (pyrophosphate) DPD (3,3-diphosphono-1,2-propanodicarboxylic acid), and HEDP (hydroxymethylene diphosphonate), have been transformative for the field of CA and nuclear cardiology as well. The mechanism of uptake of bone agents is attributed to the binding to the microcalcifications in the amyloid fibrils, especially in the ATTR-CA but, not in the AL-CA. A meta-analysis of 5 studies found a sensitivity of 92.2% and specificity of 95.4% for detecting ATTR-CA, whereas its diagnostic performance for AL amyloidosis is poor (sensitivity and specificity <50%) [91]. ATTR-CA shows higher uptake of bone tracer (Fig. 16.20) because the density of microcalcifications is greater in ATTR amyloidosis than in AL amyloidosis [109]. Binding mechanisms and the effect of fibril type on tracer affinity need to be clarified. Thus, whereas scintigraphy with the ^{99m}Tc bone-seeking tracers is a remarkably useful test for patients with suspected amyloidosis, vigilance is required to identify and further evaluate cases in which there is discordance between clinical and imaging findings [106].

[^{11}C]PiB, a derivative of thioflavin-T, has been used with success in β -amyloid imaging in neurodegenerative diseases and has also been shown to accurately identify cardiac AL-amyloidosis [110]. Thus, it may prove to be useful to monitor response to therapeutic interventions or for prognostication in the realm of cardiac amyloidosis. Pilot studies reported that ^{18}F -labeled amyloid tracers, such as [^{18}F]Florbetapir, have the potential to detect CA but, well clinical studies need to confirm the accuracy of the β -amyloid tracers for the diagnosis of CA [111].

Aprotinin (Trasylol), a small protein (6.511 kDa) bovine pancreatic trypsin inhibitor (BPTI) is an antifibrinolytic molecule that inhibits trypsin and related proteolytic enzymes. It was reported that ^{99m}Tc -aprotinin binds to amyloid deposits which contain proteases. Pilot studies documented the potential of this tracer to detect

CA. However, more studies are needed to confirm the pilot data [112, 113].

16.3.6 Cardiac Fibrosis

Fibrosis is the excessive accumulation of extracellular matrix typically found in the remodeling left ventricle, resulting from activation of cardiac fibroblasts. The feasibility of imaging matrix metalloproteinases using radiopharmaceuticals such as ^{111}In -RP782 or ^{99m}Tc -RP805, which accumulate in remodeling vasculature and myocardium has been reported. However, matrix remodeling is a relatively late pathogenetic process in ischemic heart failure progression, which may restrict the benefit for many patients [114]. Since fibroblasts comprise up to 50% of the cellular content of the heart, and fibrosis is the consequence of fibroblast activation, a promising target for molecular imaging is the fibroblast activation protein (FAP), which exhibits low expression by quiescent cardiac fibroblasts but, is rapidly upregulated in response to injury stimuli, and during fibroblast transdifferentiation [115, 116]. Also targeting activated myofibroblasts can depict the active disease at a very early stage where treatments would likely have the most benefit.

The feasibility of PET imaging of activated fibroblasts with ^{68}Ga -FAPI-04, a FAP inhibitor was first demonstrated in a preclinical model of myocardial infarction. ^{68}Ga -FAPI-04 uptake in the injured myocardium peaked on day 6 after coronary ligation. The tracer accumulated intensely in the MI territory, as identified by decreased [^{18}F]FDG uptake and confirmed by PET/MR and H&E staining [28]. Autoradiography and H&E staining of cross-sections revealed that ^{68}Ga -FAPI-04 accumulated mainly at the border zone of the infarcted myocardium (Fig. 16.21). Subsequently, several clinical studies documented the potential of ^{68}Ga labeled FAPI radiotracers to image the activated fibroblasts in the myocardium [117–120]. Figure 16.22 shows ^{68}Ga -FAPI-04 PET/CMR in a patient after myocardial infarction. Recently, another FAP-

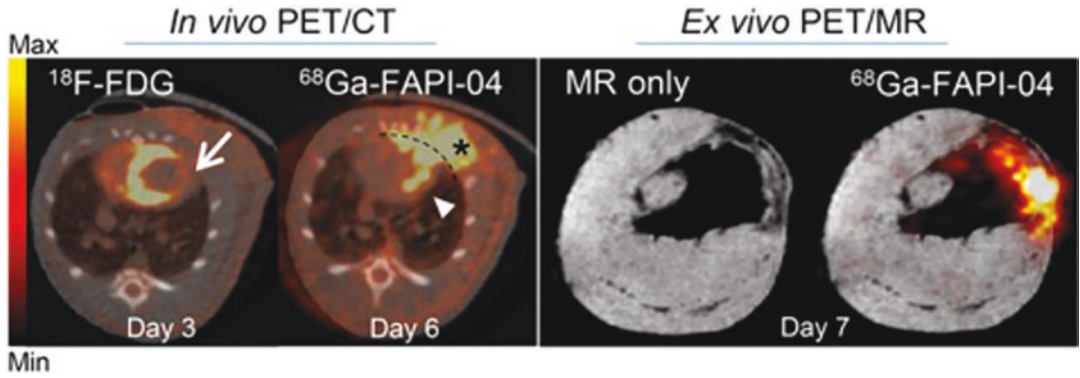


Fig. 16.21 Axial sections of in vivo PET/CT imaging with [¹⁸F]FDG (day 3 after MI) and ⁶⁸Ga-FAPI-04 (day 6 after MI) and corresponding ex vivo PET/MRI with ⁶⁸Ga-FAPI-04 (day 7 after MI). [¹⁸F]FDG image was used to identify areas of infarcted myocardium (arrow), where increased uptake of ⁶⁸Ga-FAPI-04 was apparent (arrow-

head). ⁶⁸Ga-FAPI-04 exhibited elevated uptake in postsurgical scar (asterisk). The dashed line separates ⁶⁸Ga-FAPI-04 uptake in myocardium from surgical wound. High-resolution MR and PET/MR data confirmed infarcted area, where ⁶⁸Ga-FAPI-04 uptake was increased. (From [28])

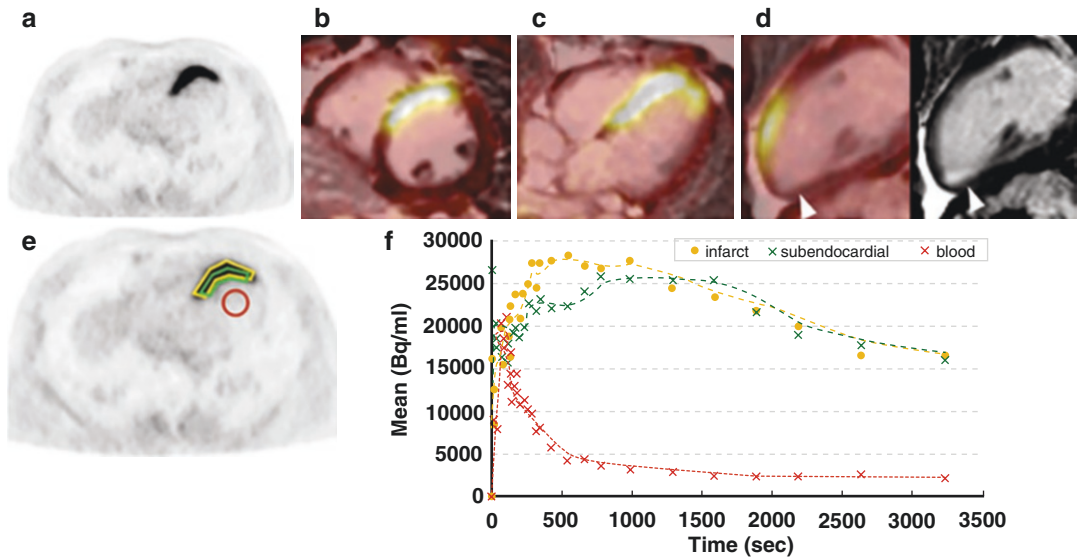


Fig. 16.22 ⁶⁸Ga-FAPI-04 PET/CMR in a patient after myocardial infarction. ⁶⁸Ga-FAPI-04 PET/CMR in a patient after acute STEMI in LAD territory and ⁶⁸Ga-FAPI-04 tracer kinetics. (a) Attenuation corrected axial PET. Fusion images of PET with 15 min late gadolinium enhancement sequences in (b) short axis, (c) horizontal long axis, and (d) vertical long axis and

corresponding MR. Arrowhead indicates small mature scar. (e) Example placement of ROI for dynamic analysis. (f) ⁶⁸Ga-FAPI-04 tracer kinetics. Intense ⁶⁸Ga-FAPI-04 uptake was observed in anterior and anterior septum wall in LAD territory. No significant ⁶⁸Ga-FAPI-04 uptake is shown in the remote area similar to blood pool [119]

targeting PET radiotracer, ⁶⁸Ga-MHLL1, was evaluated for non-invasive tracking of dynamic fibrosis in an animal model. ⁶⁸Ga-MHLL1 displayed selective binding to FAP in the infarct and infarct border zone, as well as remote non-infarcted myocardium, post-MI [121].

Dedicated prospective clinical studies are necessary to determine the added value of FAP imaging of myocardial fibrosis for predicting functional outcomes in cardiac patients.

16.3.7 Inflammation and Atherosclerosis

Atherosclerosis is a well-known disease leading to cardiovascular events, including myocardial infarction and ischemic stroke. The biology of atherosclerosis (Fig. 16.23) provides a basis for the development of radiolabeled molecular imaging probes. Fundamentally, the process of inflammation regulates atherosclerosis. Specifically, the macrophage has emerged as the key cellular mediator of inflammation in atheroma, and participates in all phases of atherogenesis, including lesion initiation, progression, and complication [14, 19, 122].

The main structural change in the vascular wall in atherosclerosis is thickening, associated with the accumulation of lipid metabolism products in the intima, the development of fibrous transformation, necrosis and calcification, and the formation of atheroma. The growth of atherosclerotic plaque over time leads to increasing stenosis of the lumen of the vessel and impaired hemodynamics, which, within certain limits, can be partially or completely compensated both by the expansion of the vessel and by the elasticity of intact sections of the walls. Rupture of the plaque capsule, with subsequent thrombosis, can lead to both acute occlusion of the vessel itself

and embolism in its distal branches, which are direct causes of vascular events. Factors leading to a decrease in blood flow in the vessel can include either an increase in the size of the plaque itself, while maintaining its integrity, or a tear or complete rupture of the capsule with subsequent thrombosis on its surface or in the resulting crater. In addition, with the fragmentation of blood clots or the plaque itself, emboli may be formed that spread with the flow of arterial blood, occluding the lumen of blood vessels distal to the plaque. Atheroma that are prone to rupture are usually referred to as vulnerable. The concept of “vulnerable plaque” was first proposed by J. Muller et al. in 1989 to designate atherosclerotic plaques that do not affect hemodynamics but, at the same time, are dangerous from the point of view of thrombosis [16, 18, 123]. Fatal myocardial infarctions or sudden cardiac death have been presented as the first manifestation of coronary artery disease without preceding ischemic symptoms. Thus, vulnerable atherosclerotic plaque, also called ‘active-forming’ or ‘rupture-prone’ plaque, needs to be discriminated from stable plaques.

Thus, the biology of the atherosclerotic lesion itself provides the basis for the development of atherosclerosis-targeted molecular imaging probes (Table 16.1). A number of noninvasive

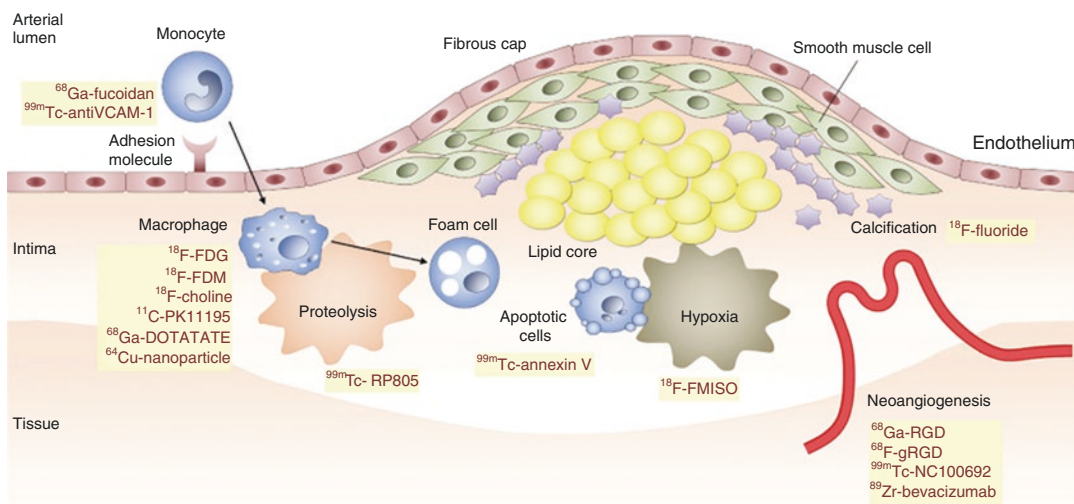


Fig. 16.23 Pathogenesis mechanism and molecular imaging targets in vulnerable plaque. (From Lee and Paeng [128])

and invasive diagnostic imaging techniques are being evaluated to accurately identify high-risk individuals, based on the presence of high-risk anatomical or structural features of atherosclerotic plaques in the coronary arteries. However, imaging coronary lesions is a challenge since they are contained within the wall of the vessel, and typically these lesions occupy a fraction of the vessel circumference and often extend from 1 to 2 cm. In addition, the residual activity of the radiotracer in blood, and the myocardial tissue uptake of the radiotracer make these lesions more difficult to detect. Molecular imaging technique based on specific β^+ emitting radiotracers, however, may provide the potential to detect coronary atherosclerotic lesions (Fig. 16.23).

16.3.7.1 Radiotracers for Vulnerable Plaque

In the 1970s it was first demonstrated that ^{125}I -labeled LDL localizes in the carotid atherosclerotic lesions in human subjects [124]. Since that time a number of radiolabeled LDL preparations, antibodies, and peptides have been extensively evaluated in animal models as potential

radiotracers for imaging atherosclerotic lesions [19]. Molecular imaging based on PET and SPECT radiotracers is a rapidly evolving discipline that aims to develop imaging agents and technologies to visualize the specific molecular processes associated with vulnerable plaque. Several reviews discussed extensively the development and evaluation of PET and SPECT radiotracers for molecules imaging of atherosclerosis and vulnerable plaque [125–131].

In the 1990s, investigators at the Mount Sinai Medical Center in New York were the first to demonstrate that FDG-PET identifies macrophage-rich atherosclerotic lesions in hypercholesterolemic rabbits (Fig. 16.24). The histopathological data also suggested that the amount of FDG uptake in the lesion correlates with the macrophage density in the lesion [132, 133]. FDG accumulation in ruptured plaques has been first confirmed in the carotids of patients who presented transient ischemic attack where symptomatic carotid artery lesions exhibited higher FDG uptake than asymptomatic lesions [134]. Ex vivo incubation of excised carotid plaques with tritiated deoxyglucose confirmed

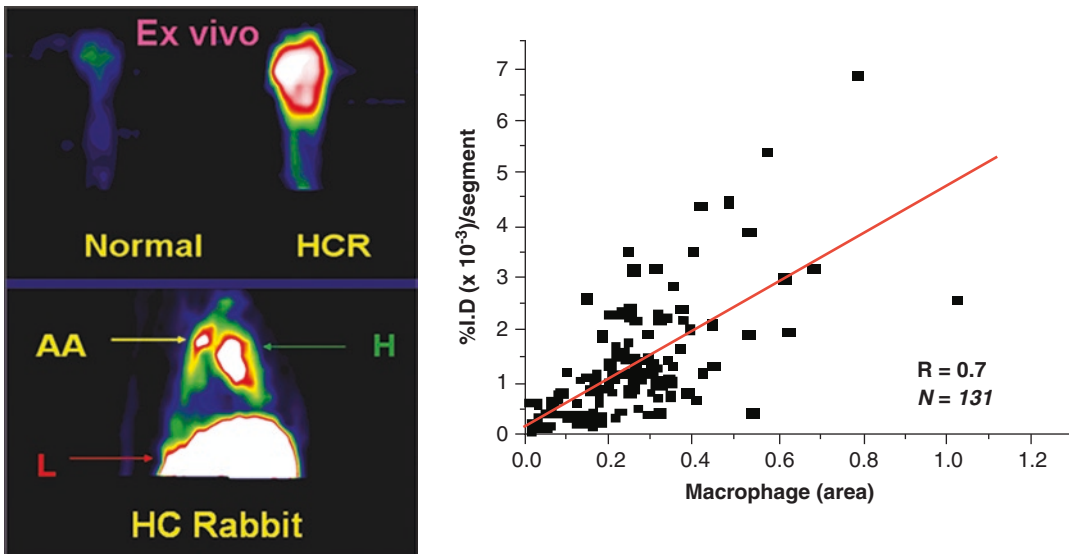


Fig. 16.24 [^{18}F]FDG-PET to image atherosclerosis in hypercholesterolemic rabbits (HCR). The bottom in vivo image shows FDG uptake in the ascending aorta (AA) of HCR while the top ex vivo image shows comparison of

HCR and normal aortas. The FDG uptake in the atherosclerotic lesions appears to depend on the macrophage density

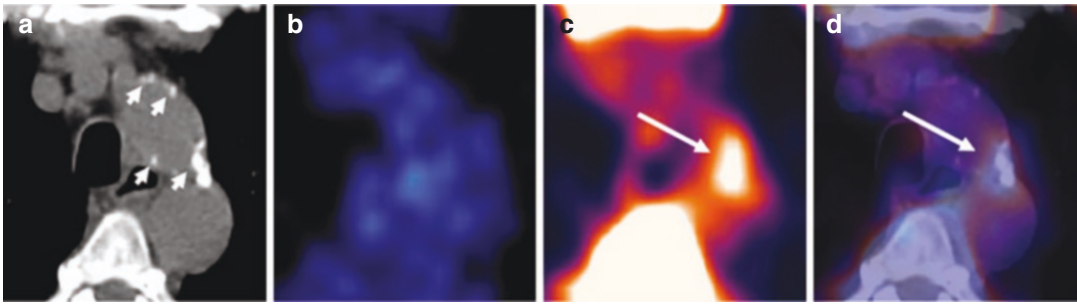


Fig. 16.25 Transaxial PET/CT images of atherosclerotic plaque in aortic arch: CT image (a), [^{18}F]FDG PET image (b), ^{18}F -fluoride PET image (c), and coregistered and fused [^{18}F]FDG/ ^{18}F -fluoride PET/CT image (d).

Accumulation of ^{18}F -fluoride is colocalized with large calcification but, not with [^{18}F]FDG uptake. Short arrow five calcifications; long arrow five tracer uptake. (From [140])

that metabolic activities in plaques have a heterogeneous distribution and concentrate predominantly within macrophage-rich areas on autoradiographs [135]. Using carotid specimens from patients who had an endarterectomy after intravenous administration of [^{18}F]FDG, microPET-MRI analysis confirmed that FDG accumulates mostly in regions of the plaque with high density of macrophages and foam cells but, also in regions with loose matrix containing activated smooth muscle cells, fibroblasts, and neovessels [136]. Subsequently, localization of FDG in human atheroma has been documented for the carotid arteries, aorta, and other major vessels [137, 138].

During the last two decades, FDG-PET imaging has emerged as a powerful tool to explore noninvasively inflammatory activities in atherosclerotic plaques providing new insights on the evolution of metabolic activities in the vascular wall over time. Vascular inflammation evaluated with FDG-PET appears to be an interesting marker of cardiovascular risk. Unlike circulating biomarkers, FDG-PET imaging provides a direct assessment of the intensity of inflammation in the vascular wall [127].

The most promising radiopharmaceutical that emerged in the past 10 years for plaque imaging is [^{18}F]sodium fluoride [^{18}F]NaF, a PET radiopharmaceutical for imaging metastatic bone lesions. [^{18}F]NaF PET/CT (Fig. 16.25) showed the potential for the imaging of arterial calcification in major arteries [139, 140]. Fluoride-PET

has the potential to detect microcalcifications located in culprit lesions or high-risk plaques. In a prospective study of 40 patients with myocardial infarction and 40 with stable angina, [^{18}F]NaF successfully identified vulnerable coronary lesions in 93% of the lesions implicated in causing the infarction [141]. Increased uptake was also observed in 45% of the patients with stable coronary artery disease being referred for invasive coronary angiography. In these patients and in 40 patients with stable angina, regions of ^{18}F uptake correlated with intravascular ultrasound findings of microcalcification, a necrotic core, and positive remodeling. A major research study CAMONA (Cardiovascular Molecular Calcification Assessed by NaF PET/CT) was conducted to compare the performance of FDG- and NaF-PET for assessing atherosclerosis. Based on the data from this study, a recent review concludes that NaF as a PET tracer will play a critical role in detecting atherosclerosis in both normal aging as well as in patients with low or high risk for this potentially fatal disease [142]. Since [^{18}F]Fluoride uptake is due to the presence of micro or macro calcifications, prospective clinical trials are needed to assess the prognostic value of [^{18}F]Fluoride-PET as a novel biomarker for plaque vulnerability.

Several other potential atherosclerotic plaque imaging agents, many of which are still in preliminary preclinical and clinical studies, have been described. Some of these approaches include somatostatin receptor (SSTR) binding

ligands (^{68}Ga -Dotatoc, ^{64}Cu -Dotatate), the integrin $\alpha_v\beta_3$ binding RGD tripeptides analogs (^{18}F -Galacto-RGD, ^{18}F -Flotegatide, ^{18}F -Fluciclatide), and translocator protein (TSPO) specific inflammation markers (^{11}C PK11195; ^{18}F JPBR-714), chemokine receptor (CXCR4) specific ligands (^{68}Ga -Pentixafor). In addition, several potential molecular imaging targets and approaches which remain relatively unexplored in atherosclerosis. As imaging instruments (PET/CT and PET/MRI) become more advanced and artificial intelligence becomes more clinically useful, investigations will continue into the selection of appropriate molecular imaging probes for atherosclerosis and vulnerable plaque.

References

- Berman DS, Shaw LJ, Hachamovitch R, et al. Comparative use of radionuclide stress testing, coronary artery calcium scanning, and noninvasive coronary angiography for diagnostic and prognostic cardiac assessment. *Semin Nucl Med.* 2007;37:2–16.
- Klein R, Celiker-Guler E, Rotstein BH, deKemp RA. PET and SPECT tracers for myocardial perfusion imaging. *Semin Nucl Med.* 2020;50:208–18.
- Schwaiger M, Bengel FM. From thallium scan to molecular imaging. *Mol Imaging Biol.* 2003;4:387–98.
- Werner RA, Thackeray JT, Diekmann J, et al. The changing face of nuclear cardiology: guiding cardiovascular care toward molecular medicine. *J Nucl Med.* 2020;61:951–61.
- Lairez O, Hyafil F, Manrique BA, et al. Assessment of coronary flow reserve in nuclear cardiology. *Évaluation de la réserve coronaire en cardiologie Nucléaire. Médecine Nucléaire.* 2020;44(3):172–80.
- Farber G, Boczar KE, Wiefels CC, et al. The future of cardiac molecular imaging. *Semin Nucl Med.* 2020;50:367–85.
- Glaserapp A, Hess A, Thackeray JT. Molecular imaging in nuclear cardiology: pathways to individual precision medicine. *J Nucl Cardiol.* 2020;27(6):2195–201.
- Moghbel M, Al-Zaghal A, Werner TJ, et al. The role of PET in evaluating atherosclerosis: a critical review. *Semin Nucl Med.* 2018;48:488–97.
- Yang M, Arsanjani R, Roarke MC. Advanced nuclear medicine and molecular imaging in the diagnosis of cardiomyopathy. *AJR.* 2020;215:1208–17.
- Libby P. Inflammation in atherosclerosis. *Nature.* 2002;420:868–74.
- Ross R. Atherosclerosis—an inflammatory disease. *N Engl J Med.* 1999;340:115–26.
- Fuster V, Moreno PR, Fayad ZA, et al. Atherothrombosis and high-risk plaque part I: evolving concepts. *J Am Coll Cardiol.* 2005;46:937–54.
- Spagnoli LG, Bonanno E, Sangiorgi G, et al. Role of inflammation in atherosclerosis. *J Nucl Med.* 2007;48:1800–15.
- Falk E. Pathogenesis of atherosclerosis. *J Am Coll Cardiol.* 2006;47:C7–12.
- Virmani R, Burke AP, Farb F, et al. Pathology of the vulnerable plaque. *J Am Coll Cardiol.* 2006;47:C13–8.
- Muller JE, Abela GS, Nesto RW, et al. Triggers, acute risk factors and vulnerable plaques: the lexicon of a new frontier. *J Am Coll Cardiol.* 1994;23:809–13.
- Moreno PR. Vulnerable plaque: definition, diagnosis, and treatment. *Cardiol Clin.* 2010;28(1):1–30.
- Muller JE, Tawakol A, Kathiresan S, et al. New opportunities for identification and reduction of coronary risk: treatment of vulnerable patients, arteries, and Plaques. *J Am Coll Cardiol.* 2006;47:C2–6.
- Vallabhajosula S, Fuster V. Atherosclerosis: imaging techniques and the evolving role of nuclear medicine. *J Nucl Med.* 1997;38:1688–96.
- Naghavi M, Libby P, Falk E, et al. From vulnerable plaque to vulnerable patient. A call for new definitions and risk assessment strategies: part I. *Circulation.* 2003;108:1664–72.
- Naghavi M, Falk E, Hecht HS, et al. From vulnerable plaque to vulnerable patient—part III: executive summary of the screening for heart attack prevention and education (SHAPE) task force report. *Am J Cardiol.* 2006;98(2A):2H–15H.
- Strauss HW, Grewal RK, Pandit-Taskar N. Molecular imaging in nuclear cardiology. *Semin Nucl Med.* 2004;34:47–55.
- Travin MI, Bergmann SR. Assessment of myocardial viability. *Semin Nucl Med.* 2005;35:2–16.
- Barron HV, Lesh MD. Autonomic nervous system and sudden cardiac death. *J Am Coll Cardiol.* 1996;27:1053–60.
- Gilotra NA, Griffin JM, Pavlovic N, et al. Sarcoidosis-related cardiomyopathy: current knowledge, challenges, and future perspectives state-of-the-art review. *J Card Fail.* 2022;28(1):113–32.
- Rubin J, Maurer MS. Cardiac amyloidosis: overlooked, underappreciated, and treatable. *Annu Rev Med.* 2020;71:203–19.
- Hara H, Takeda N, Komuro I. Pathophysiology and therapeutic potential of cardiac fibrosis. *Inflamm Regen.* 2017;37:13.
- Varasteh Z, Mohanta S, Robu S, et al. Molecular imaging of fibroblast activity after myocardial infarction using a ^{68}Ga -labeled fibroblast activation protein inhibitor, FAPI-04. *J Nucl Med.* 2019;60:1743–9.
- de Haas HJ, van den Borne SW, Boersma HH, et al. Evolving role of molecular imaging for new under-

- standing: targeting myofibroblasts to predict remodeling. *Ann NY Acad Sci.* 2012;1254:33–4.
30. Park S, Nguyen NB, Pezhouman A, Ardehali R. Cardiac fibrosis: potential therapeutic targets. *Transl Res.* 2019;209:121–37.
 31. Sogbein OO, Pelletier-Galarneau M, Schindler T. New SPECT and PET radiopharmaceuticals for imaging cardiovascular disease. *BioMed Res Int.* 2014;2014:942960.
 32. Sinusas AJ, Zaret BL. Coronary artery disease. In: Wagner HN, Szabo Z, Buchanan JW, editors. *Principles of nuclear medicine.* 2nd ed. Philadelphia: Saunders; 1995.
 33. Gould KL, Lipscomb K, Hamilton GW. Physiologic basis for assessing critical coronary stenosis: instantaneous flow response and regional distribution during coronary hyperemia as measures of coronary flow reserve. *Am J Cardiol.* 1974;33:87–94.
 34. Schelbert HR. Positron emission tomography of the heart: methodology, findings in the normal and disease heart, and clinical applications. In: Phelps ME, editor. *PET: molecular imaging and its clinical applications.* New York: Springer; 2004.
 35. Strauss HW, Harrison K, Langan JK, et al. Thallium-201 for myocardial imaging. Relation of thallium-201 to regional myocardial perfusion. *Circulation.* 1975;51:641–5.
 36. Jain D. Technetium-99m labeled myocardial perfusion imaging agents. *Semi Nucl Med.* 1999;29(3):221–236.
 37. Nitzsche EU, Choi Y, Czernin J, et al. Noninvasive quantification of myocardial blood flow in humans. A direct comparison of the [¹³N]ammonia and the [¹⁵O]water techniques. *Circulation.* 1996;93:2000–6.
 38. Kotzerke J, Glatting G, van den Hoff J, et al. Validation of myocardial blood flow estimation with nitrogen-13 ammonia PET by the argon inert gas technique in humans. *Eur J Nucl Med.* 2001;28:340–5.
 39. Machac J. Cardiac positron emission tomography imaging. *Semin Nucl Med.* 2005;35:17–36.
 40. Lin JW, Sciacca RR, Chou RL, et al. Quantification of myocardial perfusion in human subjects using ⁸²Rb and wavelet-based noise reduction. *J Nucl Med.* 2001;42:201–8.
 41. Nekolla SG, Reder S, Saraste A, et al. Evaluation of the novel myocardial perfusion positron-emission tomography tracer 18F-BMS-747158-02: comparison to ¹³N-ammonia and validation with microspheres in a pig model. *Circulation.* 2009;119(17):2333–42.
 42. Bing RJ. The metabolism of the heart. In: Harvey Society of NY, editor. *Harvey lecture series.* New York: Academic; 1954.
 43. Heineman FW, Balaban RS. Effects of after load and heart rate on NAD(P)H redox state in the isolated rabbit heart. *Am J Physiol Heart Circ Physiol.* 1993;264:H433–40.
 44. Opie LH, Owen P. Assessment of myocardial free NAD⁺/NADH ratios and oxaloacetate concentrations during increased mechanical work in isolated perfused rat heart during production or uptake of ketone bodies. *Biochem J.* 1975;148:403–15.
 45. Liedtke AJ. Alterations of carbohydrate and lipid metabolism in the acutely ischemic heart. *Prog Cardiovasc Dis.* 1981;23:321–36.
 46. Kudo T. Metabolic imaging using PET. *Eur J Nucl Med Mol Imaging.* 2007;34:S49–61.
 47. Wallhaus TR, Taylor M, DeGrado TR, et al. Myocardial free fatty acid and glucose use after carvedilol treatment in patients with congestive heart failure. *Circulation.* 2001;103:2441–6.
 48. Lopaschul GD, Stanley W. Glucose metabolism in the ischemic heart. *Circulation.* 1997;95:415–22.
 49. Phelps ME, Huang SC, Hoffman EJ, et al. Tomographic measurement of local cerebral glucose metabolic rate in humans with (F-18)2-fluoro-2-deoxy-D-glucose: validation of method. *Ann Neurol.* 1979;6:371–88.
 50. Sokoloff L, Reivich M, Kennedy C, et al. The [¹⁴C] deoxyglucose method for the measurement of local cerebral glucose utilization: theory, procedure, and normal values in the conscious and anesthetized albino rat. *J Neurochem.* 1977;28:897–916.
 51. Krivokapich J, Huang SC, Selin CE, et al. Fluorodeoxyglucose rate constants, lumped constant, and glucose metabolic rate in rabbit heart. *Am J Physiol.* 1987;252:H777–87.
 52. Botker HE, Bottcher M, Schmitz O, et al. Glucose uptake and lumped constant variability in normal human hearts determined with [¹⁸F]fluorodeoxyglucose. *J Nucl Cardiol.* 1997;4:125–32.
 53. Tillisch J, Brunken R, Marshall R, et al. Reversibility of cardiac wall-motion abnormalities predicted by positron tomography. *N Engl J Med.* 1986;314:884–8.
 54. Brinkmann JF, Abumrad NA, Ibrahim A, et al. New insights into long-chain fatty acid uptake by heart muscle: a crucial role for fatty acid translocase/CD36. *Biochem J.* 2002;367:561–70.
 55. Taki J, Matsunari I. Metabolic imaging using SPECT. *Eur J Nucl Med Mol Imaging.* 2007;34:S34–48.
 56. Tamaki N, Morita K, Kuge Y, et al. The role of fatty acids in cardiac imaging. *J Nucl Med.* 2000;41:1525–34.
 57. Schön HR, Schelbert HR, Robinson, et al. C-11 labeled palmitic acid for the noninvasive evaluation of regional myocardial fatty acid metabolism with positron-computed tomography. I. Kinetics of C-11 palmitic acid in normal myocardium. *Am Heart J.* 1982;103:532–47.
 58. Stone CK, Pooley RA, DeGrado TR, et al. Myocardial uptake of the fatty acid analog 14-fluorine-18-fluoro-6-thia-heptadecanoic acid in comparison to beta-oxidation rates by tritiated palmitate. *J Nucl Med.* 1998;39:1690–6.

59. Buckman BO, Van Brocklin HF, Dence CS, et al. Synthesis and tissue distribution of [ω - ^{11}C] palmitic acid. A novel PET imaging agent for cardiac fatty acid metabolism. *J Med Chem.* 1994;27:2481–5.
60. Taylor M, Wallhaus TR, Degradó TR, et al. An evaluation of myocardial fatty acid and glucose uptake using PET with [^{18}F]fluoro-6-thia-heptadecanoic acid and [^{18}F]FDG in patients with congestive heart failure. *J Nucl Med.* 2001;42:55–62.
61. Poe ND, Robinson GD Jr, Zielinski FW. Myocardial imaging with ^{123}I -hexadecenoic acid. *Radiology.* 1977;124:419–24.
62. Freundlieb C, Hock A, Vyska K. Myocardial imaging and metabolic studies with [16 - ^{123}I]iodohexadecanoic acid. *J Nucl Med.* 1980;21:1043–50.
63. Knapp FF Jr, Ambrose KR, Goodman MM. New radioiodinated methyl-branched fatty acids for cardiac studies. *Eur J Nucl Med.* 1986;12:S39–44.
64. Knapp FF Jr, Goodman MM, Callahan AP, et al. Radioiodinated 15-(p-iodophenyl)-3,3-dimethylpentadecanoic acid: a useful new agent to evaluate myocardial fatty acid uptake. *J Nucl Med.* 1986;27:521–31.
65. Yamamoto Y, de Silva R, Rhodes CG. Noninvasive quantification of regional myocardial metabolic rate of oxygen by $^{15}\text{O}_2$ inhalation and positron emission tomography. *Circulation.* 1996;94:808–16.
66. Tamaki N, Magata Y, Takahashi N, et al. Myocardial oxidative metabolism in normal subjects in fasting, glucose loading and dobutamine infusion states. *Ann Nucl Med.* 1992;6:221–8.
67. Armbrecht JJ, Buxton DB, Brunken RC, et al. Regional myocardial oxygen consumption determined noninvasively in human with [^{11}C]acetate and dynamic positron tomography. *Circulation.* 1989;80:863–72.
68. Sciacca RR, Akinboboye O, Chou RL, et al. Measurement of myocardial blood flow with PET using 1– ^{11}C -acetate. *J Nucl Med.* 2001;42:63–70.
69. Triposkiadis F, Karayannis G, Giamouzis G, et al. Nervous system in heart failure: physiology, pathophysiology, and clinical implications. *J Am Coll Cardiol.* 2009;2009(54):1747–62.
70. Raffel DM, Wieland DM. Assessment of cardiac sympathetic nerve integrity with positron emission tomography. *Nucl Med Biol.* 2001;28:541–59.
71. Carrio I. Cardiac neurotransmission imaging. *J Nucl Med.* 2001;42:1062–76.
72. Lautamäki R, Tipre D, Bengel FM, et al. Cardiac sympathetic neuronal imaging using PET. *Eur J Nucl Med Mol Imaging.* 2007;34:S74–85.
73. Rosenpire KC, Haka MS, Jewett DM, et al. Synthesis and preliminary evaluation of ^{11}C -methoxyephedrine: a false neurotransmitter agent for heart neuronal imaging. *J Nucl Med.* 1990;31:1328–34.
74. Wieland DM, Swanson DP, Brown LE, et al. Imaging the adrenal medulla with an I-131-labeled antiadrenergic agent. *J Nucl Med.* 1979;20:155–8.
75. Wieland DM, Brown LE, Rogers WL, et al. Myocardial imaging with a radioiodinated norepinephrine storage analog. *J Nucl Med.* 1981;22:22–31.
76. Kline RC, Swanson DP, Wieland DM, et al. Myocardial imaging with I-123-metaiodobenzylguanidine. *J Nucl Med.* 2001;22:129–32.
77. Yamashina S, Yamazaki J-I. Neuronal imaging using SPECT. *Eur J Nucl Med Mol Imaging.* 2007;34:S62–73.
78. Raffel DM, Jung Y-W, Koeppe RA, et al. First-in-human studies of [^{18}F]fluorohydroxyphenethylguanidines: PET radiotracers for quantifying regional cardiac sympathetic nerve density. *Circ Cardiovasc Imaging.* 2018;11:e007965.
79. Werner RA, Rischpler C, Onthank D, et al. Retention kinetics of the ^{18}F -labeled sympathetic nerve PET tracer LMI1195: comparison with ^{11}C -hydroxyephedrine and ^{123}I -MIBG. *J Nucl Med.* 2015;56:1429–33.
80. Zhang H, Huang R, Pillarsetty NK, et al. Synthesis and evaluation of [^{18}F]fluorine-labeled benzylguanidine analogs for targeting the human norepinephrine transporter. *Eur J Nucl Med Mol Imaging.* 2014;41(2):322–32.
81. Pandit-Taskar N, Zanzonico P, Staton KD. Biodistribution and dosimetry of ^{18}F -meta-fluorobenzylguanidine: a first-in-human PET/CT imaging study of patients with neuroendocrine malignancies. *J Nucl Med.* 2018;59(1):147–53.
82. Schaefers M, Riemann B, Levkau B, et al. Current status and future applications of cardiac receptor imaging with positron emission tomography. *Nucl Med Commun.* 2002;23:113–5.
83. Delforge J, Syrota A, Lancon JP, et al. Cardiac beta-adrenergic receptor density measured in vivo using PET, CGP12167, and a new graphical method. *J Nucl Med.* 1991;32:739–48.
84. Elsinga PH, van Waarde A, Vaalburg W. Receptor imaging in the thorax with PET. *Eur J Pharmacol.* 2004;499:1–13.
85. Werner RA, Chen X, Hirano M, et al. SPECT vs. PET in cardiac innervation imaging: clash of the titans. *Clin Transl Imaging.* 2018;6:293–303.
86. Zelt JGE, deKemp RA, Rotstein BH. Nuclear imaging of the cardiac sympathetic nervous system a disease-specific interpretation in heart failure. *JACC Cardiovasc Imaging.* 2020;13(4):1036–54.
87. Fallavollita JA, Heavey BM, Luisi AJ Jr, et al. Regional myocardial sympathetic denervation predicts the risk of sudden cardiac arrest in ischemic cardiomyopathy. *J Am Coll Cardiol.* 2014;63(2):141–9.
88. Fallavollita JA, Dare JD, Carter RL, et al. Denervated myocardium is preferentially associated with sudden cardiac arrest in ischemic cardiomyopathy: a pilot competing risks analysis of cause-specific mortality. *Circ Cardiovasc Imaging.* 2017;10(8):e006446.

89. Imamura Y, Ando H, Mitsuoka W, et al. Iodine-123 metaiodobenzylguanidine images reflect intense myocardial adrenergic nervous activity in congestive heart failure independent of underlying cause. *J Am Coll Cardiol.* 1995;26:1594–1599.
90. Dimitriu-Leen AC, Scholte AJHA, Jacobson AF. ¹²³I-MIBG SPECT for evaluation of patients with heart failure. *J Nucl Med.* 2015;56:25S–30S.
91. Hotta M, Minamimoto R, Awaya T, et al. Radionuclide imaging of cardiac amyloidosis and sarcoidosis: roles and characteristics of various tracers. *RadioGraphics.* 2020;40:2029–41.
92. Okayama K, Kurata C, Tawarahara K, et al. Diagnostic and prognostic value of myocardial scintigraphy with thallium-201 and gallium-67 in cardiac sarcoidosis. *Chest.* 1995;107(2):330–4.
93. Momose M, Kadoya M, Koshikawa M, et al. ⁶⁷Ga SPECT and integrated low-dose CT scanning (SPECT/CT) in the diagnosis of cardiac sarcoidosis. *Ann Nucl Med.* 2007;21(10):545–51.
94. Chareonthaitawee P, Beanlands RS, Chen W, et al. Joint SNMMI–ASNC expert consensus document on the role of ¹⁸F-FDG PET/CT in cardiac sarcoid detection and therapy monitoring. *J Nucl Med.* 2017;58(8):1341–53.
95. Blankstein R, Waller AH. Evaluation of known or suspected cardiac sarcoidosis. *Circ Cardiovasc Imaging.* 2016;9(3):e000867. <https://doi.org/10.1161/CIRCIMAGING.113.000867>. PMID: 26926267.
96. Norikane T, Yamamoto Y, Maeda Y, et al. ¹⁸F-FLT PET imaging in a patient with sarcoidosis with cardiac involvement. *Clin Nucl Med.* 2015;40(5):433–34.
97. Martineau P, Pelletier-Galarneau M, Juneau D, et al. Imaging cardiac sarcoidosis with FLT-PET compared with FDG/perfusion-PET: a prospective pilot study. *JACC Cardiovasc Imaging.* 2019;12(11 Pt 1):2280–1.
98. ten Bokum AM, Hofland LJ, de Jong G, et al. Immunohistochemical localization of somatostatin receptor sst2A in sarcoid granulomas. *Eur J Clin Invest.* 1999;29(7):630–6.
99. Gormsen LC, Haraldsen A, Kramer S, et al. A dual tracer ⁶⁸Ga-DOTA-NOC PET/CT and ¹⁸F-FDG PET/CT pilot study for detection of cardiac sarcoidosis. *EJNMMI Res.* 2016;6:52.
100. Kaushik P, Patel C, Gulati G, et al. Comparison of ⁶⁸Ga-DOTANOC PET/CT with cardiac MRI in patients with clinical suspicion of cardiac sarcoidosis. *Ann Nucl Med.* 2021;35:1058–65.
101. Kwekkeboom DJ, Krenning EP, Kho GS, Breeman WA, Van Hagen PM. Somatostatin receptor imaging in patients with sarcoidosis. *Eur J Nucl Med.* 1998;25(9):1284–92.
102. Lapa C, Reiter T, Kircher M, et al. Somatostatin receptor based PET/CT in patients with the suspicion of cardiac sarcoidosis: an initial comparison to cardiac MRI. *Oncotarget.* 2016;7(47):77807–14.
103. Gilstrap LG, Dominici F, Wang Y, et al. Epidemiology of cardiac amyloidosis-associated heart failure hospitalizations among fee-for-service Medicare beneficiaries in the United States. *Circ Heart Fail.* 2019;12:e005407.
104. Dorbala S, Ando Y, Bokhari S, et al. ASNC/AHA/ASE/EANM/HFSA/ISA/SCMR/SNMMI expert consensus recommendations for multimodality imaging in cardiac amyloidosis: part 1 of 2-evidence base and standardized methods of imaging. *J Card Fail.* 2019;25:e1–39.
105. Garcia-Pavia P, Rapezzi C, Adler Y, et al. Diagnosis and treatment of cardiac amyloidosis: a position statement of the ESC Working Group on Myocardial and Pericardial Diseases. *Eur Heart J.* 2021;42:1554–68.
106. Masri A, Bukhari S, Eisele YS, Soman P. Molecular imaging of cardiac amyloidosis. *J Nucl Med.* 2020;61:965–70.
107. Paeng JC, Young J. Nuclear imaging for cardiac amyloidosis: bone scan, SPECT/CT, and amyloid-targeting PET Choi2. *Nucl Med Mol Imaging.* 2021;55:61–70.
108. Pelletier-Galarneau M, Abikhzer G, Giraldeau G, Harel F. Molecular imaging of cardiac amyloidosis. *Curr Cardiol Rep.* 2019;21:12.
109. Stats MA, Stone JR. Varying levels of small microcalcifications and macrophages in ATTR and AL cardiac amyloidosis: implications for utilizing nuclear medicine studies to subtype amyloidosis. *Cardiovasc Pathol.* 2016;25(5):413–7.
110. Lee S-P, Lee ES, Choi H, et al. ¹¹C-Pittsburgh B PET imaging in cardiac amyloidosis. *JACC Cardiovasc Imaging.* 2015;8:50–9.
111. Sperry BW, Bock A, DiFilippo FP, et al. Pilot study of F18-florbetapir in the early evaluation of cardiac amyloidosis. *Front Cardiovasc Med.* 2019;8:693194.
112. Awaya T, Minamimoto R, Iwama K, et al. Performance of ^{99m}Tc-aprotinin scintigraphy for diagnosing light chain (AL) cardiac amyloidosis confirmed by endomyocardial biopsy. *J Nucl Cardiol.* 2020;27:1145–53.
113. Schaadt BK, Hendel HW, Gimsing P, et al. ^{99m}Tc-aprotinin scintigraphy in amyloidosis. *J Nucl Med.* 2003;44:177–83.
114. Thackeray JT. Molecular imaging using cardiac PET/CT: opportunities to harmonize diagnosis and therapy. *Curr Cardiol Rep.* 2021;23:96.
115. Tillmanns J, Hoffmann D, Habbaba Y, et al. Fibroblast activation protein alpha expression identifies activated fibroblasts after myocardial infarction. *J Mol Cell Cardiol.* 2015;87:194–203.
116. Varasteh Z, Weber WA, Rischpler C. Nuclear molecular imaging of cardiac remodeling after myocardial infarction. *Pharmaceuticals.* 2022;15:183.
117. Gu Y, Han K, Zhang Z, et al. FAPI PET/CT for molecular assessment of fibroblast activation in right heart in pulmonary arterial hypertension: a single-center, pilot study. *J Nucl Cardiol.* 2022.

118. Heckmann MB, Reinhardt F, Finke D, et al. Relationship between cardiac fibroblast activation protein activity by positron emission tomography and cardiovascular disease. *Circ Cardiovasc Imaging*. 2020;13(9):e010628.
119. Notohamiprodjo S, Nekolla SG, Robu S, et al. Imaging of cardiac fibroblast activation in a patient after acute myocardial infarction using ⁶⁸Ga-FAPI-04. *J Nucl Cardiol*. 2022;29(5):2254–61.
120. Siebermair J, Kohler MI, Kupusovic J, et al. Cardiac fibroblast activation detected by Ga-68 FAPI PET imaging as a potential novel biomarker of cardiac injury/remodeling. *J Nucl Cardiol*. 2021;28(3):812–21.
121. Langer LB, Hess A, Korkmaz Z, et al. Molecular imaging of fibroblast activation protein after myocardial infarction using the novel radiotracer [⁶⁸Ga] MHL. *Theranostics*. 2021;11:7755–66.
122. Jaffer FA, Libby P, Weissleder R. Molecular and cellular imaging of atherosclerosis. *Emerging applications*. *J Am Coll Cardiol*. 2006;47:1328–38.
123. Fuster V, Corti R, Fayad ZA, et al. Integration of vascular biology and magnetic resonance imaging in the understanding of atherothrombosis and acute coronary syndromes. *J Thromb Haemost*. 2003;1:1410–21.
124. Lees RS, Lees AM, Strauss HW. External imaging of human atherosclerosis. *J Nucl Med*. 1983;24:154–6.
125. Anzola LK, Rivera JN, Ramirez JC. Molecular imaging of vulnerable coronary plaque with radiolabeled somatostatin receptors (SSTR). *Clin Med*. 2021;10:5515.
126. Krishnan S, Otaki Y, Doris M, et al. Molecular imaging of vulnerable coronary plaque: a pathophysiological perspective. *J Nucl Med*. 2017;58:359–64.
127. Lairez O, Hyafil F. A clinical role of PET in atherosclerosis and vulnerable plaques? *Semin Nucl Med*. 2020;50:311–8.
128. Lee SJ, Paeng JC. Nuclear molecular imaging for vulnerable atherosclerotic plaques. *Korean J Radiol*. 2015;16(5):955–66.
129. MacAskill MG, Newby DE, Tavares AAS. Frontiers in positron emission tomography imaging of the vulnerable atherosclerotic plaque. *Cardiovasc Res*. 2019;115(14):1952–62.
130. Nakahara T, Narula J, Strauss W. Molecular imaging of vulnerable plaque. *Semin Nucl Med*. 2018;48(3):291–8.
131. Migdalski A, Jawien A. New insight into biology, molecular diagnostics and treatment options of unstable carotid atherosclerotic plaque: a narrative review. *Ann Transl Med*. 2021;9(14):1207–18.
132. Vallabhajosula S, Machac J, Knesaurek K, et al. Imaging atherosclerotic lesions by PET using [¹⁸F]fluorodeoxyglucose (FDG): preclinical studies in hypercholesterolemic rabbits. *Circulation*. 1995;92:313.
133. Vallabhajosula S, Machac J, Knesaurek K, et al. Imaging atherosclerotic macrophage density by positron emission tomography using [¹⁸F]fluorodeoxyglucose (FDG). *J Nucl Med*. 1996;37:38p.
134. Rudd JH, Warburton EA, Fryer TD, et al. Imaging atherosclerotic plaque inflammation with [¹⁸F]-fluorodeoxyglucose positron emission tomography. *Circulation*. 2002;105:2708–11.
135. Masteling MG, Zeebregts CJ, Tio RA, et al. High-resolution imaging of human atherosclerotic carotid plaques with micro ¹⁸F-FDG PET scanning exploring plaque vulnerability. *J Nucl Cardiol*. 2011;18:1066–75.
136. Liu J, Kerwin WS, Caldwell JH, et al. High resolution FDG-microPET of carotid atherosclerosis: plaque components underlying enhanced FDG uptake. *Int J Cardiovasc Imaging*. 2016;32:145–52.
137. Ben-Haim S, Israel O. PET/CT for atherosclerotic imaging. *Q J Nucl Med Mol Imaging*. 2006;50:53–60.
138. Weissberg PL. Noninvasive imaging of atherosclerosis: the biology behind the pictures. *J Nucl Med*. 2004;45:1974–695.
139. Derlin T, Richter U, Bannas P, et al. Feasibility of ¹⁸F-sodium fluoride PET/CT for imaging of atherosclerotic plaque. *J Nucl Med*. 2010;51:862–5.
140. Derlin T, Tóth Z, Papp L, et al. Correlation of inflammation assessed by ¹⁸F-FDG PET, active mineral deposition assessed by ¹⁸F-fluoride PET, and vascular calcification in atherosclerotic plaque: a dualtracer PET/CT study. *J Nucl Med*. 2011;2011(52):1020–7.
141. Joshi NV, Vesey AT, Williams MC, et al. ¹⁸F-fluoride positron emission tomography for identification of ruptured and high-risk coronary atherosclerotic plaques: a prospective clinical trial. *Lancet*. 2014;383:705–13.
142. Alavi A, Werner TJ, Raynor W, et al. Critical review of PET imaging for detection and characterization of the atherosclerotic plaques with emphasis on limitations of FDG-PET compared to NaF-PET in this setting. *Am J Nucl Med Mol Imaging*. 2021;11(5):337–51.